Final Year Design 20/21

Reactor Design Report

COLOSSEUM STEELWORKS - TEAM 3

Colosseum
Steelworks

Binti Ahmad Dzulfakhar, Aiman Syahirah
Charaschanya, Theeranai
Charos, Athanasios
Duru, Naomi
Khan, Fatima Elzahra
Lee, Seyoung
Sim, En You
Tonus, Alessandro
Walker, Pierre
Woolley, Richard

Chapter 2

Process Design of Key Reactor Unit

Contents

Nomenclature

Table 2.0.1: Variables

Symbol	Description	Units
α	EXAMPLE SYMBOL	m^{10}
m_{SM}	Mass of Solid Metal Zone	kg
m_{LM}	Mass of Liquid Metal Zone	kg
m_{SSl}	Mass of Solid Slag Zone	kg
m_{LSl}	Mass of Liquid Slag Zone	kg
m_{Gas}	Mass of Gas Zone	kg
T_{SM}	Temperature of Solid Metal Zone	K
T_{LM}	Temperature of Liquid Metal Zone	K
T_{SSl}	Temperature of Solid Slag Zone	K
T_{LSl}	Temperature of Liquid Slag Zone	K
T_{Gas}	Temperature of Gas Zone	K
$m_{i,SM}$	Mass of Component i in Solid Metal Zone	kg
$m_{i,LM}$	Mass of Component i in Liquid Metal Zone	kg
$m_{i,SSl}$	Mass of Component i in Solid Slag Zone	kg
$m_{i,LSl}$	Mass of Component i in Liquid Slag Zone	kg
$m_{i,Gas}$	Mass of Component i in Gas Zone	kg
Q_{Arc}	Energy Dissipated from the Electric Arcs by Conduction	kW
Q_{LM-SM}	Conduction between the Solid Metal Zone and Liquid Metal Zone	kW
Q_{SM-SSl}	Conduction between Solid Metal Zone and Solid Slag Zone	kW
Q_{SM-LSl}	Conduction between Solid Metal Zone and Liquid Slag Zone	kW
Q_{SM-Gas}	Convection between Solid Metal Zone and Gas Zone	kW
$Q_{SM-Water}$	Cooling of Solid Metal Zone Through Furnace Wall	kW
Q_{LM-SSl}	Conduction between Liquid Metal Zone and Solid Slag Zone	kW
Q_{LM-LSl}	Conduction between Liquid Metal Zone and Liquid Slag Zone	kW
Q_{LM-Gas}	Convection between Liquid Metal Zone and Gas Zone	kW
$Q_{LM-Water}$	Cooling of Liquid Metal Zone Through Furnace Wall	kW
$Q_{SSl-Water}$	Cooling of Solid Slag Zone Through Furnace Wall	kW
$Q_{LSl-Gas}$	Convection between Liquid Slag Zone and Gas Zone	kW
$Q_{LSl-Water}$	Cooling of Liquid Slag Zone Through Furnace Wall	kW
$Q_{Arc-Gas}$	Energy Received by Gas Zone from Electric Arcs	kW
$Q_{Gas-Water}$	Energy Loss of Gas Zone Through Furnace Wall	kW
K_{SM-LM}	Exposure Coefficient Between Solid Metal Zone and Liquid Metal Zone	$-$

Table 2.0.2: Parameters

Symbol	Description	Value	Units
r_{C-L}	Injected C Decarburization Rate[1]	15	$kg\ s^{-1}$
r_{C-D}	Dissolved C Decarburization Rate[1]	35	$kg\ s^{-1}$
r_{C-1}	C Oxidation to CO Rate[1]	60	$kg\ s^{-1}$
r_{C-2}	C Oxidation to CO_2 Rate[1]	55	$kg\ s^{-1}$
r_{Mn-1}	MnO Decarburization Rate[1]	20	$kg\ s^{-1}$
r_{Mn-2}	Si with MnO Rate[1]	10	$kg\ s^{-1}$
r_{Mn}	Mn with FeO Rate[1]	75	$kg\ s^{-1}$
r_{Si-1}	Si Desiliconization Rate[1]	144	$kg\ s^{-1}$
r_{Si-2}	Si Oxidation to SiO_2 Rate[1]	250	$kg\ s^{-1}$
r_{Cr-1}	Cr with Feo Rate[1]	3	$kg\ s^{-1}$
r_{Cr-2}	Cr Oxidation Rate[1]	1	$kg\ s^{-1}$
r_P	P Oxidation Rate[1]	35	$kg\ s^{-1}$
r_{comb}	C_9H_{20} Combustion Rate[1]	0.1	s^{-1}
K_{HT1}	SM-LM Heat Transfer Coefficient[2]	0.2	$kW\ m^{-2}\ K^{-1}$
K_{HT2}	SM-SSl Heat Transfer Coefficient[2]	0.2	$kW\ m^{-2}\ K^{-1}$
K_{HT3}	SM-LSl Heat Transfer Coefficient[2]	0.05	$kW\ m^{-2}\ K^{-1}$
K_{HT4}	SM-Gas Heat Transfer Coefficient[2]	57.5	$kW\ K^{-1}$
K_{HT5}	LM-SSl Heat Transfer Coefficient[2]	0.2	$kW\ m^{-2}\ K^{-1}$
K_{HT6}	LM-LSl Heat Transfer Coefficient[2]	0.08	$kW\ m^{-2}\ K^{-1}$
K_{HT7}	LM-Gas Heat Transfer Coefficient[2]	22.5	$kW\ K^{-1}$
K_{HT8}	LSl-Gas Heat Transfer Coefficient[2]	22.5	$kW\ K^{-1}$
K_{A1}	SM-LM Area Coefficient[2]	0.008	$m^2\ kg^{-1}$
K_{A2}	SM-SSl Area Coefficient[2]	0.12	$m^2\ kg^{-1}$
K_{A3}	SM-LSl Area Coefficient[2]	0.12	$m^2\ kg^{-1}$
K_{A5}	LM-SSl Area Coefficient[2]	0.12	$m^2\ kg^{-1}$
K_{A6}	LM-LSl Area Coefficient[2]	0.12	$m^2\ kg^{-1}$
K_{W1}	SM-Water Thermal Conductance Coefficient[2]	12	$kW\ K^{-1}$
K_{W2}	LM-Water Thermal Conductance Coefficient[2]	20	$kW\ K^{-1}$
K_{W3}	SSl-Water Thermal Conductance Coefficient[2]	10	$kW\ K^{-1}$
K_{W4}	LSl-Water Thermal Conductance Coefficient[2]	5	$kW\ K^{-1}$
K_{W5}	Gas-Water Thermal Conductance Coefficient[2]	0.05	$kW\ K^{-1}$
m_{EAF}	Mass Capacity of EAF	180000	kg
T_{Melt}	Melting Temperature of Steel[2]	1809	K

2.1 Introduction

The process outlined by Colosseum Steelworks incorporates a total of seven reactors, all of which are crucial to the chemical looping scheme within the process. This set of reactors consists of three reducer units, an oxidizer unit, an air reactor unit, a hydrogen burner and an electric arc furnace. The reducers serve to reduce iron ore, primarily hematite (Fe_2O_3), to iron whereas the oxidiser oxidises iron to magnetite (Fe_3O_4) and the air reactor subsequently oxidizes magnetite to reproduce hematite. The hydrogen burner is used to power a Rankine cycle. The electric arc furnace (EAF) is then used to convert the direct reduced iron (DRI) produced from the core chemical looping process along with steel scrap into the final steel product. The reactor sizes for all the reactors excluding the EAF can be found in Appendix 2.7.8.

2.1.1 Justification for Selecting EAF as Detailed Reactor

The EAF was selected as the reactor to be designed in detailed for three key reasons - the importance of the reactor in the overall process, the complexity of the model and the innovative nature of operation. The EAF is not only a high energy-consuming process, but is also responsible for CO_2 emissions, both directly through the off-gas produced and indirectly through the arc electricity requirement. Although the indirect emissions from the electricity are mitigated through the use of a steam turbine for power generation, the direct CO_2 emissions from the EAF go to a gas flare. In fact, all the direct CO_2 produced in the upstream chemical looping process has been captured for storage, so the direct CO_2 emissions from the overall process are solely from the EAF, thus requiring careful consideration and minimisation. The EAF is also responsible for ensuring that the final steel product, the medium-carbon steel, fits the composition purity requirements. In terms of complexity, the EAF involves a large number of reactions whereby all reactions play a key role in determining the final product composition. Furthermore, unlike the other reactors, there are more than two input streams and two output streams associated with the EAF. Complications also arise due to the mass and heat transfer between the different phases (solid, liquid and gas) present within the reactor, making it an interesting process to model. Colosseum Steelworks also aims to operate the EAF in a continuous fashion, using an expired patent by Danieli Corporation[3] as a guideline. The first reason for operating continuously is to convert the DRI from the upstream chemical looping process into liquid steel seamlessly. This is beneficial from a thermal efficiency standpoint because operating the reactor in a batch process scheme would require cooling of DRI, subsequent of storage DRI, and then reheating the DRI before feeding into the EAF. Another key reason to opt for continuous operation is the environmental damage caused by releasing carbon monoxide to the atmosphere in a batch process, where the EAF roof has to be opened after every run to insert hot briquetted iron (HBI).

2.1.2 Alternatives to EAF

The blast oxygen furnace (BOF) is the melting technology that acts as the primary alternative to the EAF. This is because it is often integrated with a blast furnace, and hence is an important reactor for the majority of global steel production. However, as demonstrated in the TOPSIS and AHP analysis conducted in Section 1.2.2, EAF outperforms BOF from an environmental, process novelty and safety perspective, while only losing out in terms of overall economics and technological readiness. The decarbonisation potential of the EAF also suggests that it is the melting technology that best fits with Colosseum Steelworks' priorities.

2.2 Model

There have been several attempts to model an EAF using various simplifications in literature. Colosseum Steelworks decided to primarily base the detailed EAF model on the one proposed in the set of papers published by Logar *et al.*[1,2], as this is the most complete approach found in literature that has been experimentally validated with operational data. The model itself can be split into three major components - heat transfer element, mass transfer element and thermo-chemical element, all of which when put together, represent the dynamic behaviour of the EAF. Although the paper is relatively self-contained, there are key issues and distinctions that needed to be addressed in order to design an EAF that is suitable for the purposes of Colosseum Steelworks' process. One of the key differences from the paper was the removal of methane

injection to EAF oxygen burners in order to heat-up the solid metal, as the majority of the feed is already heated up from the upstream process. The paper's simplification of neglecting impurities was also amended so that mass and mole fractions sum to unity. Additionally, the relationships for the equilibrium molar fractions were taken from the respective sources rather than using the simplified correlations presented in the paper. Lastly and most importantly, the paper outlines the model for a batch system but Colosseum Steelworks' plant aims to use a continuous EAF system so the convergent solution was used to guide the steady state behaviour of the proposed continuous feeding system.

2.2.1 Key Assumptions

To obtain a robust model, several assumptions were made when developing the mass transfer and heat transfer relationships for the EAF. The primary reason for this is the presence of inherent randomness in the process that cannot be modelled by conventional laws. This model is time-variant, consisting of a combination of first-order differential equations and other algebraic relationships, solved using the fixed-step forward Euler method with a time interval of 10^{-3} s. In addition, discontinuities were modelled such that no instability issues occurred. The EAF is divided into different homogeneous zones where the components in each zone have identical chemical, thermal and physical properties. This assumption makes it simpler to model the relationships between different phases (solid, liquid and gas) present in the system. The different zones are shown in Fig. 2.2.1, and are explained below.
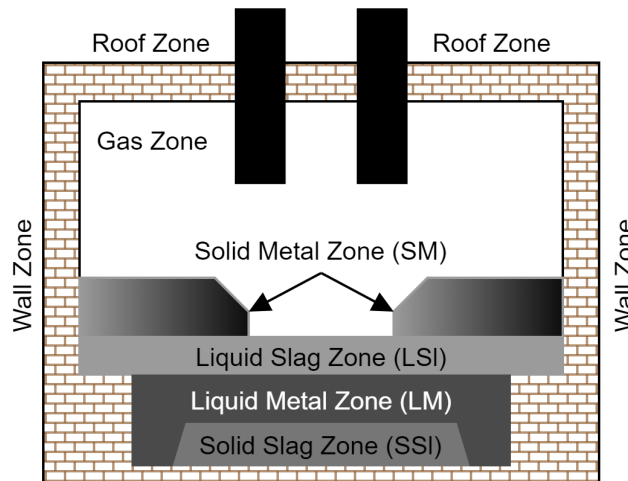

Figure 2.2.1: Key EAF Homogeneous Zones for Modelling Purposes

- Solid Metal Zone (SM): Contains individual elements in their solid form, specifically Fe, C, Mn, Si, Cr and P. The paper by Logar et $al.$[2] assumes a scrap steel input that contains no oxides and only the elements mentioned above, along with combustible hydrocarbon residues approximated as C_9H_{20}, whereas the process at hand has a hot direct reduced iron feed that does contain oxide impurities. As a result, the oxide impurities of the hot iron feed consisting of SiO_2, Al_2O_3, MnO, MgO, CaO and P_2O_5 have been included in this zone. The solid elements in this zone will melt into the liquid metal zone, while these oxide impurities will melt into the liquid slag zone rather than the liquid metal zone. The presence of Na_2O, K_2O, Zn and Pb in the hot metal feed are neglected as they are present in trace amounts and not involved in any of the chemical reactions within the model.
- Liquid Metal Zone (LM): Contains the same elements as the solid metal zone but this zone does not include the oxide impurities.
- Solid Slag Zone (SSl): Contains the added slag-forming compounds fed to the EAF in solid form on a semi-continuous basis, and contains primarily CaO and MgO, with small amounts of SiO_2 and Al_2O_3.
- Liquid Slag Zone (LSl): Contains the melted slag-forming compounds and other oxides from oxidation reactions all in liquid form, specifically FeO, CaO, MgO, SiO_2, Al_2O_3, MnO, Cr_2O_3 and P_2O_5.
- Gas Zone (Gas): The gas zone contains the gases lanced into the system and the gases produced as a result of the oxidation and reduction reactions. An assumption made is that all reactions involving air

leaks and reactions with leak air are neglected because clear details of hatches and leak area locations and sizes are not given in the paper by Logar *et al.*[2]. Therefore, the only means of gas escape is through the off-gas vent where it will be sent to a gas flare. Consequently, the EAF is assumed to be sealed such that no atmospheric air enters the system. Although other assumptions could have been used, the fact that nitrogen is not involved in any of the reactions justifies this decision. To ensure consistency of assumptions within the model, the hole radius is set equal to the electrode radius in regards to reactor geometry within the model. The gases included are therefore CO, CO_2, O_2 and H_2O, as these are the ones involved in the reactions.

- Roof Zone (Roof): Required to satisfy energy balance through conduction and radiation heat transfer. This zone contains panels that serve to cool inner contents using cooling water.
- Wall Zone (Wall): Required to satisfy energy balance through conduction and radiation heat transfer. This zone also contains contains panels that serve to cool inner contents using cooling water.

2.2.2 Heat Transfer

The EAF model consists of all three mechanisms of heat transfer: conduction, convection and radiation.
- Conduction occurs between zones that are in direct contact with one another.
- Convection occurs between the gas zone and the surrounding zones.
- Radiation occurs between zones depending on the value of the view factor.

2.2.2.1 Solid Metal

The heat fluxes through the solid metal zone include the following: electric arcs (Q_{Arc}), liquid metal (Q_{LM-SM}), liquid slag (Q_{SM-LSI}), gas (Q_{SM-Gas}), CO post-combustion ($Q_{CO-Post}$) and radiative energy (Q_{SM-Rad}). The solid metal zone also exchanges heat with the solid slag (Q_{SM-SSI}) and loses heat to the water-cooled furnace walls ($Q_{SM-Water}$). The overall heat balance for the solid metal zone is as follows.

$$Q_{SM} = Q_{LM-SM} + (1-K_{SM-LM}) \cdot (Q_{Arc} + Q_{CH_4} + K_{Post}Q_{CO-Post})$$
$$-Q_{SM-SSI} - Q_{SM-LSI} - Q_{SM-Gas} - Q_{SM-Water} - Q_{SM-Rad}. \tag{2.1}$$

The energy transferred to the solid metal zone from the electric arc through conduction is assumed to be 20% of the arc power, as per findings by Y.N. Toulouevski *et al.*[4].

$$Q_{Arc} = 0.2 \cdot P_{Arc}. \tag{2.2}$$

The terms outlined below are between the solid metal zone and the liquid metal zone, the solid slag zone and the liquid slag zone respectively. These are represented using a simple conduction relationship comprising the product of a mass term, heat transfer coefficient term, area coefficient term and the appropriate temperature difference.

$$Q_{LM-SM} = \min(m_{LM}, m_{SM}) \cdot K_{HT1}K_{A1} \cdot (T_{LM} - T_{SM}). \tag{2.3}$$

$$Q_{SM-SSI} = \min(m_{SM}, m_{SSI}) \cdot K_{HT2}K_{A2} \cdot (T_{SM} - T_{SSI}). \tag{2.4}$$

$$Q_{SM-LSI} = \min(m_{SM}, m_{LSI}) \cdot K_{HT3}K_{A3} \cdot (T_{SM} - T_{LSI}). \tag{2.5}$$

The energy transferred between the solid metal and the gas is represented by a similar relationship to Eq. 2.3, Eq. 2.4 and Eq. 2.5. The differences are the inclusion of an exposure coefficient K_{SM-LM}, and a mass ratio term to take into account the decreasing energy exchange to the gas zone as the solid metal mass decreases.

$$Q_{SM-Gas} = \frac{m_{SM}}{m_{EAF}} \cdot K_{HT4} \cdot (1-K_{SM-LM}) \cdot (T_{SM} - T_{Gas}). \tag{2.6}$$

The energy lost to the cooled furnace walls from the solid metal zone is modelled using a thermal conductance coefficient, K_{W1}, and consists of an exponential term representing the decrease in cooling as the mass of the solid metal decreases.

$$Q_{\text{SM-Water}} = K_{W1} \cdot (T_{SM} - T_{Wall}) \cdot \frac{T_{SM}}{T_{Melt}} \cdot \left(1 - \exp\left(-\frac{m_{SM}}{m_{EAF}}\right)\right). \tag{2.7}$$

2.2.2.2 Liquid Metal

Similar to the solid metal zone, the liquid metal zone receives heat from the electric arcs (Q_{Arc}), CO post-combustion ($Q_{CO-Post}$), radiation (Q_{LM-Rad}) and from the chemical reactions that take place in the furnace ($Q_{LM-Chem}$). Energy is lost to the solid metal (Q_{LM-SM}), the solid slag (Q_{LM-SSI}), the liquid slag (Q_{LM-LSI}), the gas (Q_{LM-Gas}) and the furnace walls ($Q_{LM-Water}$). The overall heat balance for the liquid metal zone is as follows:

$$Q_{LM} = Q_{LM-Chem} + (K_{SM-LM}) \cdot (Q_{Arc} + K_{Post}Q_{CO-Post})$$
$$- Q_{LM-SM} - Q_{LM-SSI} - Q_{LM-LSI} - Q_{LM-Gas} - Q_{LM-Water} - Q_{LM-Rad}. \tag{2.8}$$

Once again, the conduction relationships between the slag phases and liquid metal are represented as follows:

$$Q_{LM-SSI} = \min(m_{LM}, m_{SSI}) \cdot K_{HT5} K_{A5} \cdot (T_{LM} - T_{SSI}). \tag{2.9}$$

$$Q_{LM-LSI} = \min(m_{LM}, m_{LSI}) \cdot K_{HT6} K_{A6} \cdot (T_{LM} - T_{LSI}). \tag{2.10}$$

In addition, the energy transferred between the liquid metal and the gas includes the exposure coefficient K_{SM-LM}, and a mass ratio term to take into account the increasing energy exchange to the gas zone as the liquid metal mass increases.

$$Q_{LM-Gas} = \frac{m_{LM}}{m_{EAF}} \cdot K_{HT7} \cdot K_{SM-LM} \cdot (T_{SM} - T_{Gas}). \tag{2.11}$$

Finally, the energy lost to the cooled furnace walls from the liquid metal zone is modelled using a thermal conductance coefficient, K_{W2}, and consists of an exponential term representing the increase in cooling as the mass of the liquid metal increases.

$$Q_{LM-Water} = K_{W2} \cdot (T_{LM} - T_{Wall}) \cdot \frac{T_{LM}}{T_{Melt}} \cdot \left(1 - \exp\left(-\frac{m_{LM}}{m_{EAF}}\right)\right). \tag{2.12}$$

2.2.2.3 Solid Slag

The solid slag only interacts with the liquid metal, solid metal and cooled furnace wall, as it is not in direct contact with any other zone. The solid slag receives heat from the liquid metal (Q_{LM-SSI}), exchanges heat with the solid metal (Q_{SM-SSI}), and loses heat to the cooled-walls ($Q_{SSI-Water}$). The overall heat balance for the solid slag zone is as follows:

$$Q_{SSI} = Q_{SM-SSI} + Q_{LM-SSI} - Q_{SSI-Water}. \tag{2.13}$$

The term that is unaccounted for is the loss of heat to the cooled furnace walls, which is modelled using an exponential term to represent the decrease in cooling as the mass of the solid slag decreases:

$$Q_{\text{SSI-Water}} = K_{W3} \cdot (T_{SSI} - T_{Wall}) \cdot \frac{T_{SSI}}{T_{Melt}} \cdot \left(1 - \exp\left(-\frac{m_{SSI}}{m_{EAF}}\right)\right). \tag{2.14}$$

2.2.2.4 Liquid Slag

The liquid slag receives heat from the liquid metal (Q_{LM-LSI}), while it loses energy to the gas ($Q_{LSI-Gas}$), solid metal (Q_{SM-LSI}) and cooled furnace walls ($Q_{LSI-Water}$). Radiative energy has been neglected as it is not feasible to determine accurate radiative relations between liquid slag and other surfaces. The overall heat balance for the liquid slag zone is as follows:

$$Q_{LSI} = Q_{SM-LSI} + Q_{LM-LSI} - Q_{LSI-Gas} - Q_{LSI-Water}. \tag{2.15}$$

4

Once again, the energy transferred between the liquid slag and the gas includes the exposure coefficient K_{SM-LM}, and a mass ratio term to take into account the increasing energy exchange to the gas zone as the liquid slag mass increases.

$$Q_{LSl-Gas} = \frac{m_{LSl}}{m_{EAF}} \cdot K_{HT8} \cdot K_{SM-LM} \cdot (T_{LSl} - T_{Gas}). \tag{2.16}$$

The loss of heat to the cooled furnace walls is modelled using an exponential term to represent the increase in cooling as the mass of the liquid slag increases.

$$Q_{\text{LSl-Water}} = K_{W4} \cdot (T_{LSl} - T_{Wall}) \cdot \frac{T_{LSl}}{T_{Melt}} \cdot \left(1 - \exp\left(-\frac{m_{LSl}}{m_{EAF}}\right)\right). \tag{2.17}$$

2.2.2.5 Gas

The surrounding gas receives energy from the following: electric arcs ($Q_{Arc-Gas}$) and CO post-combustion ($Q_{CO-Post}$), while exchanging energy between the liquid metal (Q_{LM-Gas}), the solid metal (Q_{SM-Gas}) and the liquid slag ($Q_{LSl-Gas}$). It also loses energy to the furnace walls ($Q_{Gas-Water}$). The solid slag has no relation to the gas zone as it is usually small and is placed at the bottom of the furnace. The overall heat balance for the gas zone is as follows:

$$Q_{Gas} = Q_{Arc-Gas} + (1 - K_{Post})Q_{CO-post} + Q_{SM-Gas} + Q_{LM-Gas} + Q_{LSl-Gas} - Q_{Gas-Water}. \tag{2.18}$$

The assumption by Logar *et al.*[2] is that 2.5% of the electric arc power heats the gas zone.

$$Q_{Arc-Gas} = 0.025 \cdot P_{Arc}. \tag{2.19}$$

The energy lost to the cooling from the furnace walls and furnace roof is described below using a thermal conductance coefficient K_{W5}.

$$Q_{\text{Gas-Water}} = K_{W5}\left((T_{Gas} - T_{Roof})\frac{A_{Roof}}{A_{Roof} + A_{Wall}} + (T_{Gas} - T_{Wall})\frac{A_{Wall}}{A_{Roof} + A_{Wall}}\right). \tag{2.20}$$

2.2.2.6 Radiative Heat Transfer

In terms of radiation, the EAF is assumed to contain 5 surfaces as part of a set i - roof, walls, solid metal (SM), liquid metal (LM) and the electric arcs. All surfaces except the electric arcs are assumed to be gray bodies, while the electric arcs are assumed to be a transparent black body. The radiosity J_i of the gray bodies are represented in Eq. 2.21 where the first part of the equation is the Stefan-Boltzmann law and the second part represents the total incident radiation from the all other surfaces per unit of surface area i.

$$J_i = \varepsilon_i \sigma T_i^4 + (1 - \varepsilon_i) \sum_j (F_{i-j} \cdot J_j). \tag{2.21}$$

It is assumed that the solid metal and the liquid metal predominantly transfer heat through conduction such that radiative heat transfer between them can be neglected.

$$J_{Roof} = \varepsilon_{Roof} \sigma T_{Roof}^4 + (1 - \varepsilon_{Roof}) \cdot (F_{Roof-Wall} J_{Wall} + F_{Roof-SM} J_{SM} + F_{Roof-LM} J_{LM} + F_{Roof-Arc} J_{Arc}), \tag{2.22}$$

$$J_{Wall} = \varepsilon_{Wall} \sigma T_{Wall}^4 + (1 - \varepsilon_{Wall}) \cdot (F_{Wall-Roof} J_{Roof} + F_{Wall-SM} J_{SM} + F_{Wall-LM} J_{LM} + F_{Wall-Arc} J_{Arc}), \tag{2.23}$$

$$J_{SM} = \varepsilon_{SM} \sigma T_{SM}^4 + (1 - \varepsilon_{SM}) \cdot (F_{SM-Roof} J_{Roof} + F_{SM-Wall} J_{Wall} + F_{SM-Arc} J_{Arc}), \tag{2.24}$$

$$J_{LM} = \varepsilon_{LM} \sigma T_{LM}^4 + (1 - \varepsilon_{LM}) \cdot (F_{LM-Roof} J_{Roof} + F_{LM-Wall} J_{Wall} + F_{LM-Arc} J_{Arc}). \tag{2.25}$$

The energy transferred from the electric arc through radiation is assumed to be 75% of the arc power, as per findings by Y.N. Toulouevski *et al.*[4]. The remaining 2.5% is neglected as heat lost to the electrodes.

$$Q_{Arc-Rad} = 0.75 \cdot P_{Arc}. \tag{2.26}$$

The general equation for the radiative heat transfer for surface i is calculated using the radiosities of the different surfaces.

$$Q_{i-Rad} = A_i \sum_{j=1}^{N} F_{i-j}(J_i - J_j). \tag{2.27}$$

Using Eq. 2.26, the remaining radiative heat transfer terms for each surface can be obtained.

$$Q_{Roof-Rad} = A_{Roof} \cdot (F_{Roof-Wall}(J_{Roof} - J_{Wall}) + F_{Roof-SM}(J_{Roof} - J_{SM}) + F_{Roof-LM}(J_{Roof} - J_{LM}))$$
$$- F_{Arc-Roof}Q_{Arc-Rad}, \tag{2.28}$$

$$Q_{Wall-Rad} = A_{Wall} \cdot (F_{Wall-Roof}(J_{Wall} - J_{Roof}) + F_{Wall-SM}(J_{Wall} - J_{SM}) + F_{Wall-LM}(J_{Wall} - J_{LM}))$$
$$- F_{Arc-Wall}Q_{Arc-Rad}, \tag{2.29}$$

$$Q_{SM-Rad} = A_{SM} \cdot (F_{SM-Roof}(J_{SM} - J_{Roof}) + F_{SM-Wall}(J_{SM} - J_{Wall})) - F_{Arc-SM}Q_{Arc-Rad}, \tag{2.30}$$

$$Q_{LM-Rad} = A_{LM} \cdot (F_{LM-Roof}(J_{LM} - J_{Roof}) + F_{LM-Wall}(J_{LM} - J_{Wall})) - F_{Arc-LM}Q_{Arc-Rad}. \tag{2.31}$$

In order to calculate the view factors, the surfaces were approximated as basic individual geometric shapes or a combination of these, with different spatial orientations. This is because the view factors change as a result of the geometric ratios changing during the operation of the furnace. As per the detailed view factor analysis conducted by Logar *et al.*[5] in a separate paper, the roof was assumed to be a ring, the wall and electric arc as cylinders, the solid metal zone as a cone frustum and the liquid metal zone as a disc. The four phases of operation outlined by Logar *et al.*[5] for a batch melting process in the EAF include:

1. The electrodes 'drill' into the solid metal, creating a cone frustum-shaped void. The void's radius eventually reaches the walls.
2. The cone frustum-shaped void moves downwards, exposing more of the wall's surface.
3. Once a significant amount of solid metal melts, the arcs are exposed to the liquid metal, increasing the radiative flow to the liquid metal drastically, while swiftly decreasing the energy flow to the solid metal.
4. Once all the metal is molten, the slag foaming process begins.

Since the EAF is operated continuously for this process, the view factors are assumed to only consider phase 3 (arc exposure to liquid metal) and phase 4 (slag foaming). The assumption to have phase 3 represent steady state behaviour is valid because the cone frustum-shaped void will not shrink significantly with continuous operation, but rather fluctuate such that the liquid metal is continually exposed. Fig. 2.2.2 below indicates the key parameters used to determine changing view factor behaviour, with some parameters treated as constant. The detailed view factor equations used to dynamically model the process can found in Appendix 2.7.1. The inclusion of slag foaming within the model is important because slag foaming protects the electrodes and refractories from thermal radiation and minimises heat loss from the electric arc. Slag foaming refers to the production of CO bubbles. The first means of production is through the reduction reaction between wustite (FeO) and injected or dissolved carbon. It can also be formed through the reaction between injected oxygen with the dissolved carbon. A factor $(1 - K_{slag})$ is used to multiply with view factors $F_{Arc-Roof}$ and $F_{Arc-Wall}$ as a means of decreasing the view factors as the foaming slag height increases. A detailed explanation of the slag foaming model is outlined in Appendix 2.7.2.
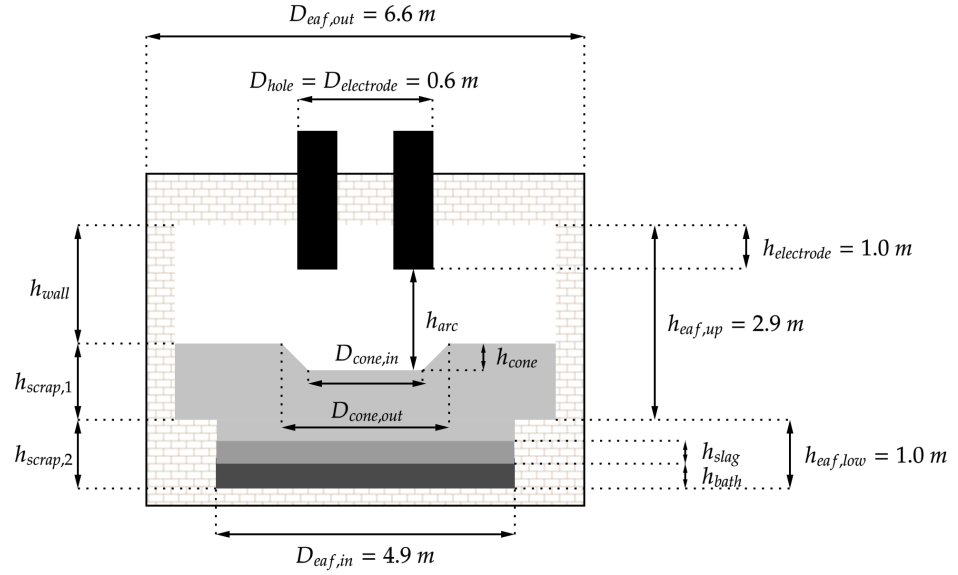
Figure 2.2.2: Key Dimensions for EAF View Factor Calculations

2.2.2.7 Temperature Change

The relationship between energy and temperature change for each EAF zone is derived from fundamental heat transfer laws. The temperature ratio factors present in the solid zone relationships are used to ensure that the temperature of the those zones do not exceed the melting point temperature. The constants ϕ_{Roof-H_2O} and ϕ_{Wall-H_2O} are the cooling water flowrates behind the panels on the roof and wall respectively.

$$\frac{dT_{SM}}{dt} = \frac{Q_{SM}\left(1-\frac{T_{SM}}{T_{Melt}}\right)}{m_{SM}C_{p,SM}} \tag{2.32}$$

$$\frac{dT_{LM}}{dt} = \frac{Q_{LM}}{m_{LM}C_{p,LM}} \tag{2.33}$$

$$\frac{dT_{SSI}}{dt} = \frac{Q_{SSL}\left(1-\frac{T_{SSI}}{T_{Melt}}\right)}{m_{SSI}C_{p,SSI}} \tag{2.34}$$

$$\frac{dT_{LSI}}{dt} = \frac{Q_{LSI}}{m_{LSI}C_{p,LSI}} \tag{2.35}$$

$$\frac{dT_{Gas}}{dt} = \frac{Q_{Gas}}{m_{Gas}C_{p,Gas}} \tag{2.36}$$

$$\frac{dT_{Roof}}{dt} = \frac{-Q_{Roof-Rad}+\frac{A_{Roof}}{A_{Roof}+A_{Wall}}\cdot Q_{Gas-Water}-\phi_{Roof-H_2O}\cdot C_{p,H_2O}\cdot\left(T_{Roof}-T_{H_2O-in}\right)}{A_{Roof}\cdot d_{Roof}\cdot\rho_{Roof}\cdot C_{p,Roof}} \tag{2.37}$$

$$\frac{dT_{Wall}}{dt} = \frac{-Q_{Wall-Rad}+\frac{A_{Wall}}{A_{Roof}+A_{Wall}}\cdot Q_{Gas-Water}-\phi_{Wall-H_2O}\cdot C_{p,H_2O}\cdot\left(T_{Wall}-T_{H_2O-in}\right)}{A_{Wall}\cdot d_{Wall}\cdot\rho_{Wall}\cdot C_{p,Wall}} \tag{2.38}$$

The temperature change due to mass addition into the system from the continuous feed is not accounted for in the equations shown above. This includes the continuous addition of direct reduced iron, scrap steel, slag forming materials, ferromanganese, carbon and oxygen. Logar et al.[2] models the change to the temperature of each zone through mass addition by interpolating between temperature of the existing zone and temperature of the entering material, as per Eq. 2.39. The equation assumes constant heat capacities and perfect mixing. This is a fair assumption for the model because the solid metal and liquid metal will have almost same heat capacities and compared to other time scales in the process, the mixing will be virtually instantaneous.

$$T_j = \frac{T_j m_j + T_{Add} m_{Add}}{m_j + m_{Add}} \qquad j=\{Zone\}, \ Add=\{Mass\ Type\}. \tag{2.39}$$

2.2.3 Mass Transfer

2.2.3.1 Mass of Zones

The total mass of each zone is made up of the respective components within the zone.

$$m_{SM} = \sum_{i \in S_{SM}} m_{i,SM} \qquad S_{SM} = \{Fe, C, Mn, Si, Cr, P, SiO_2, Al_2O_3, MnO, MgO, CaO, P_2O_5\ C_9H_{20}\},$$

(2.40)

$$m_{LM} = \sum_{i \in S_{LM}} m_{i,LM} \qquad S_{LM} = \{Fe, C, Mn, Si, Cr, P\}, \tag{2.41}$$

$$m_{SSI} = \sum_{i \in S_{SSI}} m_{i,SSI} \qquad S_{SSI} = \{CaO, MgO, SiO_2, Al_2O_3\}, \tag{2.42}$$

$$m_{LSI} = \sum_{i \in S_{LSI}} m_{i,LSI} \qquad S_{LSI} = \{FeO, CaO, MgO, SiO_2, Al_2O_3, MnO, Cr_2O_3, P_2O_5\}, \tag{2.43}$$

$$m_{Gas} = \sum_{i \in S_{Gas}} m_{i,Gas} \qquad S_{Gas} = \{CO, CO_2, O_2, H_2O\}. \tag{2.44}$$

2.2.3.2 Mass Addition/Subtraction

Mass addition to each component in each zone either through direct reduced iron, scrap steel addition, ferromanganese addition, slag forming material addition, O_2 lancing, O_2 post-combustion and C injection is factored in through the simple relationship below in Eq. 2.45. As the composition of the continuously added materials significantly affect both the reaction rates and final steel product quality, their compositions were obtained from both literature and real operations where applicable. Specifically, high carbon ferromanganese and carbon injections are needed to increase the manganese and carbon composition of the liquid steel product to meet the purity requirement. The typical slag forming additive is dolomite, where compositions were taken from Bekker et al.[6]. Finally, the scrap steel composition was taken to be the same as that presented by Logar et al.[1], as this was derived from industrial operations. Specific composition details of these inputs into the reactor can be found in Appendix 2.7.4. On the other hand, the composition of the DRI was determined by the upstream chemical looping process.

$$m_{i,j} = m_{i,j} + m_{Add,i,j} \qquad i = \{Components\}, j = \{Zone\} \tag{2.45}$$

2.2.3.3 Mass Changes from Chemical Reactions

The changes in mass for each component within their respective zones occur due to the reactions taking place in the EAF, as per Eq. 2.46. The $\dot{m}$ term refers to the change, which may be positive or negative depending on if the component is produced or consumed.

$$m_{i,j} = m_{i,j} + \dot{m}_{i,j}\Delta t \qquad i = \{Components\}, j = \{Zone\} \tag{2.46}$$

2.2.3.4 Melting Rates

Using the heat transfer equations established above, the mass transfer relationships can be constructed. The melt rate of the solid metal is given below, along with the corresponding liquid metal rate, which is equal and opposite.

$$\dot{m}_{SM} = -\frac{Q_{SM} \cdot \frac{T_{SM}}{T_{Melt}}}{\lambda_{SM} + C_{p,SM} \cdot (T_{Melt} - T_{SM})}, \tag{2.47}$$

$$m_{SM} = m_{SM} + \dot{m}_{SM}\Delta t, \tag{2.48}$$

$$\dot{m}_{LM} = -\dot{m}_{SM} \tag{2.49}$$

$$m_{LM} = m_{LM} + \dot{m}_{LM}\Delta t. \tag{2.50}$$

Similarly, the melt rate of the solid slag is given below, along with the corresponding liquid slag rate, which is equal and opposite.

$$\dot{m}_{SSI} = \frac{Q_{SSI} \cdot \frac{T_{SSI}}{T_{Melt}}}{\lambda_{SSI} + C_{p,SSI} \cdot (T_{Melt} - T_{SSI})},$$ (2.51)

$$m_{SSI} = m_{SSI} + \dot{m}_{SSI} \Delta t,$$ (2.52)

$$\dot{m}_{LSI} = -\dot{m}_{SSI},$$ (2.53)

$$m_{LSI} = m_{LSI} + \dot{m}_{LSI} \Delta t.$$ (2.54)
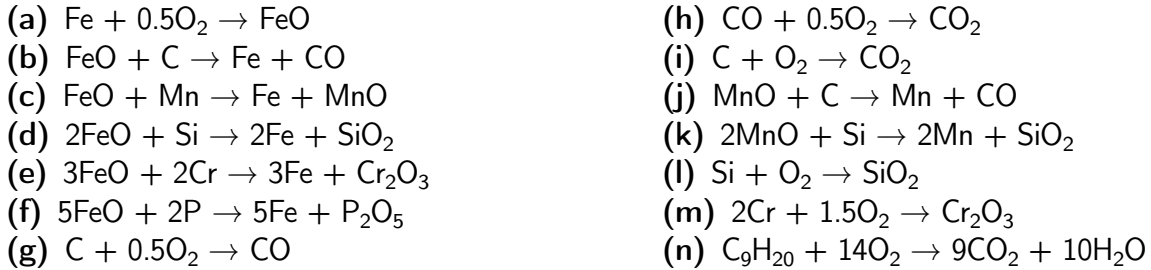
2.2.3.5 Relative Pressure

The relative pressure r_p of the EAF is made up of two terms: the first term represents the change in the number moles of gas in the system, while the second term represents the change in the temperature of the gas zone T_{Gas}.

$$r_P = \frac{R_{Gas} T_{Gas}}{V_{Gas}} \left(\frac{\dot{m}_{CO}}{M_{CO}} + \frac{\dot{m}_{CO_2}}{M_{CO_2}} + \frac{\dot{m}_{N_2}}{M_{N_2}} + \frac{\dot{m}_{O_2}}{M_{O_2}} \right) + \frac{R_{Gas} \dot{T}_{Gas}}{V_{Gas}} \left(\frac{m_{CO}}{M_{CO}} + \frac{m_{CO_2}}{M_{CO}} + \frac{m_{N_2}}{M_{N_2}} + \frac{m_{O_2}}{M_{O_2}} \right).$$ (2.55)

2.2.4 Thermo-Chemical Model

2.2.4.1 Reactions

The oxidation and reduction reactions that are considered are based upon the significance of their impact on the overall energy balance of the EAF. The model assumes that all reactions take place in the liquid metal and liquid slag zones, except the CO post-combustion. Reactions are listed below from **(a)** to **(n)**. The detailed individual reaction rates retrieved by Logar et al.[1] for each component can be found in Appendix 2.7.5.

(a) $Fe + 0.5O_2 \rightarrow FeO$

(b) $FeO + C \rightarrow Fe + CO$

(c) $FeO + Mn \rightarrow Fe + MnO$

(d) $2FeO + Si \rightarrow 2Fe + SiO_2$

(e) $3FeO + 2Cr \rightarrow 3Fe + Cr_2O_3$

(f) $5FeO + 2P \rightarrow 5Fe + P_2O_5$

(g) $C + 0.5O_2 \rightarrow CO$

(h) $CO + 0.5O_2 \rightarrow CO_2$

(i) $C + O_2 \rightarrow CO_2$

(j) $MnO + C \rightarrow Mn + CO$

(k) $2MnO + Si \rightarrow 2Mn + SiO_2$

(l) $Si + O_2 \rightarrow SiO_2$

(m) $2Cr + 1.5O_2 \rightarrow Cr_2O_3$

(n) $C_9H_{20} + 14O_2 \rightarrow 9CO_2 + 10H_2O$

2.2.4.2 Reaction Enthalpies

The general equation for the enthalpy of each reaction is shown in Eq. 2.56 below. Reaction **(o)** represents graphite electrode oxidation. The detailed reaction enthalpy equations can be found in Appendix 2.7.4.1.

$$\Delta H_T^\circ = \sum \Delta H_{298}^\circ (Products) - \sum \Delta H_{298}^\circ (Reactants)$$

$$+ \int_{298}^{T} \left[\sum C_p (Products) - \sum C_p (Reactants) \right] dT,$$ (2.56)

$$Q_{LM-Chem} = \sum_i \Delta H_{T-\textbf{SET,i}}^\circ - \Delta H_{T-\textbf{(h)}}^\circ \qquad \textbf{SET,i} = \{(a),...,(o)\},$$ (2.57)

$$Q_{CO-Post} = \Delta H_{T-\textbf{(h)}}^\circ.$$ (2.58)

2.3 Results & Further Analysis

2.3.1 Initial Results

The initial model of the EAF was developed in MATLAB based on approximate parameter values derived from operating conditions similar to that of industrial EAFs. The steel grade produced by Colosseum Steelworks is a medium-carbon steel, with specific purity requirements listed in Table 2.3.1.

Table 2.3.1: Medium-carbon Steel Purity Requirements[7,8]

| C	Mn	S	P
0.48 - 0.55	0.60 - 0.99	$\leq$0.050	$\leq$0.040

To obtain a viable operating point, operating parameters were adjusted using trial and error until the purity requirements of the final product were met at 18 cycles (3 hours) after the start of operation to demonstrate a reliable representation of long-term continuous operation. The key operating parameter for the initial model is shown in Table 2.3.2. According to the results of the initial model, despite achieving the minimum composition and production requirement of the liquid steel, there is still room for optimization. A good example of this is the unnecessarily high temperature of the liquid metal, which is around 200K higher than the melting temperature of iron, which suggests reaction rates and thermal input can be optimised further. It may also be possible to reduce the material addition requirements, decrease carbon emissions, and potentially improve selectivity of Fe to FeO.

Table 2.3.2: Key Data from Initial Model

Operating Parameters of Initial Model					
C Injection (kg/s)	Ferromanganese (kg/s)	O_2 Lance (kg/s)	O_2 Post-combustion (kg/s)	Arc Power (MW)	Slag Forming (kg/s)
0.3	1.5	4.0	1.0	40	3.0
Liquid Metal Outlet					
Flowrate (t/hr)	Temperature (K)	%C	%Mn	%Si	%P
391.5	2047	0.52	0.7	0.19	0.006
Liquid Slag Outlet					
%CaO	%MgO	%SiO$_2$	%Al$_2$O$_3$	%MnO	%FeO
14.1	10.1	40.8	27.3	5.7	5.8
Gas Outlet					
Flowrate (kg/hr)	Temperature (K)	%CO	%CO$_2$	%H$_2$O	-
3843	1800	8.7	86.2	5.1	-

2.3.2   Model Validation

Model validation was conducted prior to initiating reactor optimisation to ensure that the constructed model is in line with that proposed by Logar *et al.*[1,2]. One of the key reasons that highlights the validity of Logar *et al.*'s model is the fact that the results demonstrated good agreement with actual EAF operation. The exact details of the operation itself can be found in the original paper, but the key results from this study are represented by the dotted lines present in Fig. 2.3.1 below.

(a) Validation of Mass Change

(b) Validation of Temperature Change
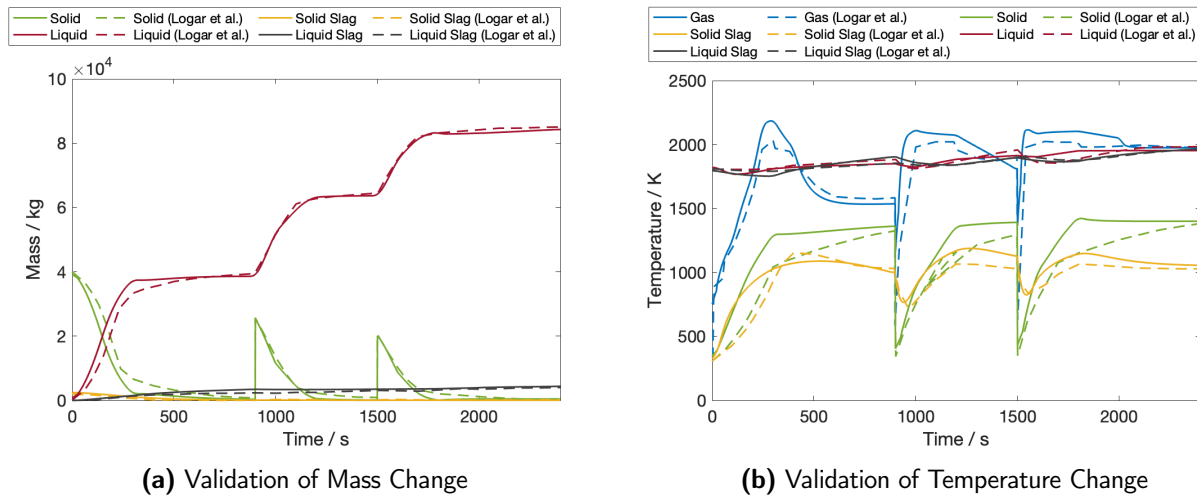
Figure 2.3.1: Result of model validation (Solid and Liquid Refers to Solid Metal and Liquid Metal Respectively)

It is important to note that the model validation can only be conducted by running the model in batch operation, so that it can be compared to Logar *et al.*'s results. The results of current model are represented

with solid lines in Fig. 2.3.1, and have been superimposed with the literature results for ease of visual comparison. Generally speaking, the results from the model developed by Colosseum Steelworks show reasonable agreement with the results derived from literature, especially in terms of the overall shape and values at convergence. At first glance, the slight deviations can be explained by different simplifications and adjustments made to the present model that differ from the original assumptions made in Logar *et al.*'s model. Firstly, the Colosseum Steelworks model is designed to deal with a continuously operating EAF, where the mass of the solid metal zone is significantly less than the reactor capacity. Therefore, the assumption regarding geometry is that the solid metal zone is treated as a cone frustum around the wall of the chamber, where the heat transfer from the arc is less significant. However, this approach is not applicable for the batch operation described in the literature as the excess solid metal would try to fill up the entire space available.

With regards to attempting to replicate the literature model for purposes of validation, specific parameters relating to the transition of the solid metal zone between phases of operation were not provided in the paper by Logar *et al.*. Therefore, three different melting algorithms were tested based on the diagrams provided in the paper - solid metal zone as a disc, solid metal zone as a cone frustum with fixed ratio of between radii and depth, and solid metal zone as a cone frustum with fixed radii. From these tests, the geometry of the solid metal was assumed to be a disc that lowers in level as the solid melts, since it provided the best agreement with the literature model results. As a consequence of this assumption, the exposure coefficient (K_{SM-LM}) of solid metal was overestimated and the heat transferred to the solid metal zone was greater. This explains the higher melting rate and higher temperature of solid metal at the initial melting phase. Moreover, the increased heat transfer through conduction from solid metal zone caused the solid slag to have a higher temperature and the liquid metal to have a lower temperature than in the original model. Additionally, the discontinuities occurring at the phase change are explained by the manual switch of view factor and phase geometry after a sufficient degree of melting was achieved (300 seconds). Finally, the model in literature assumes an open-air environment where both the presence of nitrogen and the probability of open-air reactions and leakages affect reaction rates in the model. On the contrary, the sealed environment assumed for the Colosseum Steelworks model does not take into account any interactions with atmospheric air. Therefore, the temperature change of the gas zone fluctuated more than that of Logar *et al.*'s model. Since the Colosseum Steelworks EAF operates continuously, the accuracy of the steady-state values after long-term operation is critical. Therefore, the fact that the model shows good agreement at the region of convergence indicates that the constructed model is a suitable representation of a continuously operating EAF.

2.3.3 Sensitivity Analysis

To conduct an effective sensitivity analysis, the effect of changing 9 different process parameters on a total of 6 performance indicators was investigated. The process parameters are listed below, and were varied by 20% in either direction from the nominal values in the initial model in increments of 10%. As the oxygen lancing rate parameter was particularly sensitive to various performance measures, the increment was reduced to 5% for this parameter.

1. Carbon Injection Rate
2. Ferromanganese Injection Rate
3. Oxygen Lancing Rate
4. Oxygen Post-combustion Rate
5. Slag-forming Agent Addition Rate
6. Product Removal Interval
7. Arc Power
8. Reactor Shell Upper Chamber Size
9. Reactor Shell Lower Bath Size

The effect of these 9 different process parameters were observed on the following 6 KPIs (Key Performance Indicators) that take into account composition requirements, emissions and operational efficiency.

1. Carbon Composition in Liquid Metal
2. Manganese Composition in Liquid Metal
3. Liquid Metal Outlet Temperature
4. Selectivity of Fe
5. Carbon Oxide Emissions
6. CO_2:CO Ratio

To ensure consistency among all the sensitivity experiments and to demonstrate sufficiently convergent

behaviour, each experimental run was simulated for an additional 5 operating cycles with the respective change in parameter.
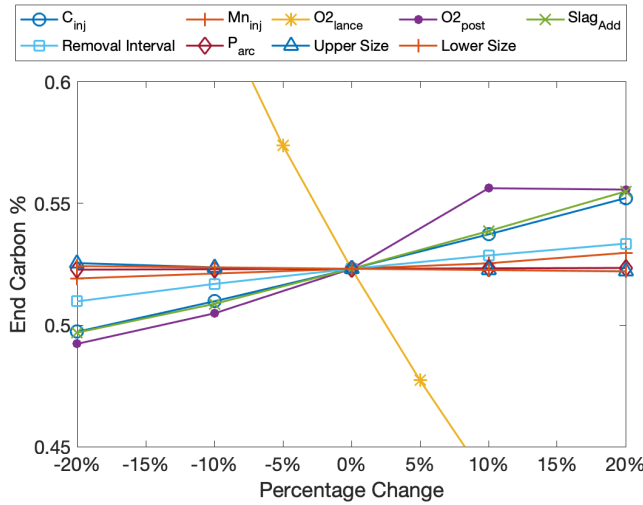
2.3.3.1 Carbon Composition

Figure 2.3.2: Sensitivity on Outlet Carbon Composition

The carbon composition of the steel product is extremely sensitive to variations in the oxygen lancing rate as a higher oxygen lancing rate causes increased oxidation of metals, especially FeO, increasing the decarburisation rate of the dissolved carbon, thus reducing the final carbon composition present in the liquid metal.

The oxygen post-combustion rate also contributes towards the carbon composition as it determines the partial pressure of carbon monoxide. This partial pressure directly affects the thermodynamic equilibrium of the decarburisation of metal oxides. Similarly, the slag forming agent addition rate also affects the activities of metal oxides present in the slag zone, thereby affecting the corresponding equilibrium mole fractions and altering the rates of the decarburisation reactions.

In conclusion, it is essential that the system is optimised in such a way that inputs into the system such as oxygen, slag-forming materials and carbon, are minimised while achieving the desired ratio to meet the carbon purity requirement.

2.3.3.2 Manganese Composition

The relationship between increasing the oxygen lancing rate showed a negative correlation with the liquid metal manganese composition because increased oxygen causes more manganese to oxidise. Similarly, oxygen addition for post-combustion also demonstrated the same behaviour as the altered partial pressure of CO shifted the thermodynamic equilibrium of manganese decarburisation. Adjusting the carbon injection also had a relatively significant positive impact on the final manganese composition, as increasing carbon in the system favors the decarburisation reaction with manganese oxide to form more manganese. As with the end product carbon composition, it is essential that the system is optimised in such a way that inputs into the system such as oxygen, slag-forming materials and carbon, are minimised while achieving the desired ratio to meet the man-

Figure 2.3.3: Sensitivity on Outlet Manganese Composition

ganese purity requirement. In particular, adjusting both the oxygen lancing rate and oxygen post-combustion rate must be conducted carefully as they did not strictly show linear behaviour in the range considered for the sensitivity analysis.
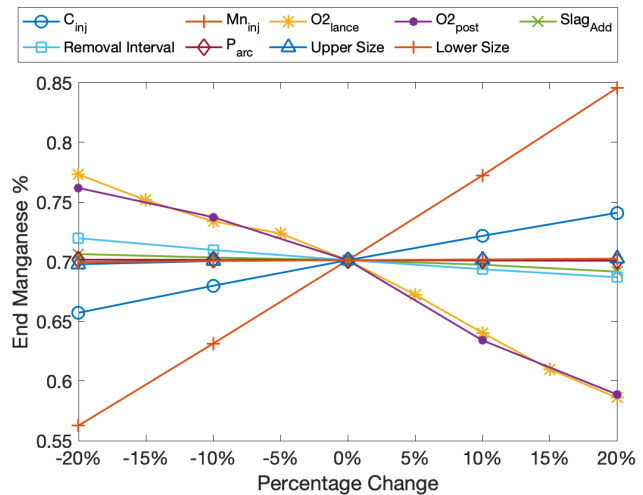
2.3.3.3 Outlet Temperature

The control of liquid metal outlet temperature is important because operating at too a high temperature within the reactor indicates that energy inefficiencies exist in the system. Inversely, an outlet temperature that is too low could lead to excess accumulation of solid metal within the system. The assumption of a closed system with regards to atmospheric gas interaction explains why the outlet temperature of the liquid metal is particularly sensitive to the size of the furnace shell. Decreasing the surface area of the roof and the walls leads to an overall decrease in the cooling water panels present, thus increasing the temperature of the liquid metal.

Moreover, less volume in the gas zone, especially in the case for decreased upper chamber size, causes the gas zone to exhibit a higher rise in temperature, subsequently decreasing the heat

Figure 2.3.4: Sensitivity on Outlet Temperature

lost through convection. One aspect to note, however, is that the effect of furnace shell sizes seem to be more drastic due to the individual scaling of the upper and lower shells sizes. This occurs because of the significant changes in the view factors. Therefore, careful adjustment of furnace size while maintaining an appropriate ratio is required to produce a desired outlet liquid metal temperature. Both oxygen lancing rate and oxygen post-combustion rate also significantly affect the final outlet temperature as nearly all of the reactions carried out by the addition of oxygen into the system are exothermic. Therefore, additional oxygen provides an extra thermal load. To conclude, it is important that the outlet temperature of the liquid metal is controlled by finding a good balance between oxygen addition, reactor size and arc power, as the initial model currently has extra heat generation highlighted by the outlet temperature which is 200 K greater than the melting point of iron.
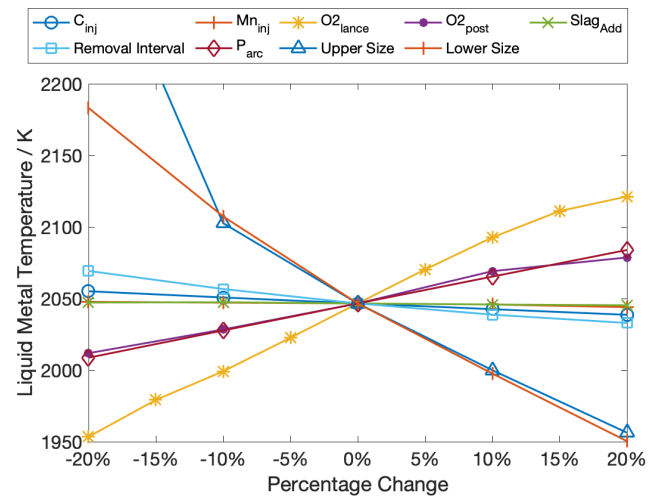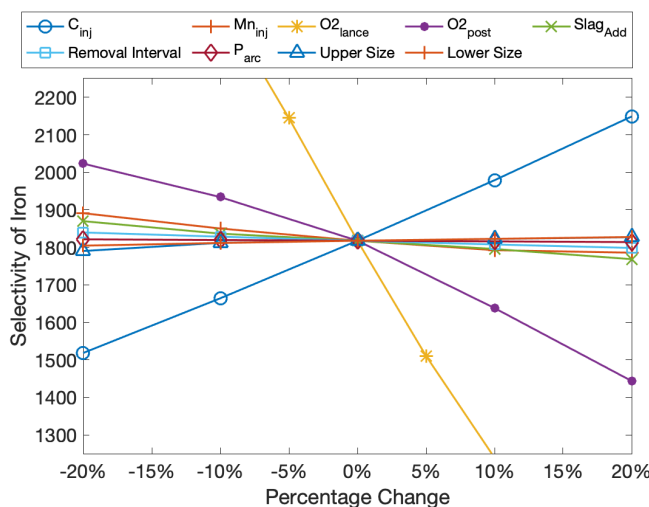
2.3.3.4 Selectivity of Fe

Figure 2.3.5: Sensitivity on Selectivity of Fe

Selectivity of iron is another important measure of efficiency since minimising conversion of iron to FeO is beneficial in terms of maximising the production and overall economic viability of the process. Since oxygen lancing contributes towards the production of FeO, a negative correlation between the oxygen lancing rate and selectivity of iron was observed. Carbon injection is another factor that contributes directly towards the decarburisation reaction, in which carbon reacts with FeO in order to produce carbon monoxide. Therefore, a linear and positive relationship between the carbon injection rate and selectivity of iron was observed. Finally, the oxygen post-combustion rate also affects the selectivity as the partial pressure of carbon monoxide affects the equilibrium mole fraction of carbon, and hence the rate of decarburisation with FeO.

2.3.3.5 Carbon Oxides Emission

A strong positive correlation between the oxygen lancing rate and the emission of carbon oxides was observed. This is due to oxygen lancing producing more metal oxides which in turn enhances the rates of various decarburisation reactions of metals. Therefore, more oxidation of dissolved carbon takes place. Additionally, the rate of slag addition and carbon injection both contribute to the shift of the equilibrium of metal oxide decarburisation reactions, and so have a minor effect on the carbon oxide emissions.

Moreover, the effect of the oxygen post combustion rate is interesting to observe since there are two opposing factors that explain the non-linear shape of the graph. The carbon oxides produced from the decarburisation reaction in liquid metal zone are affected by both the partial pressure of CO in gas zone and the tendency of the remaining oxygen in gas zone to react with the combustibles and the graphite electrode to produce carbon oxides. Therefore, it is essential to find a good balance between these two contributing factors to minimise the emissions.
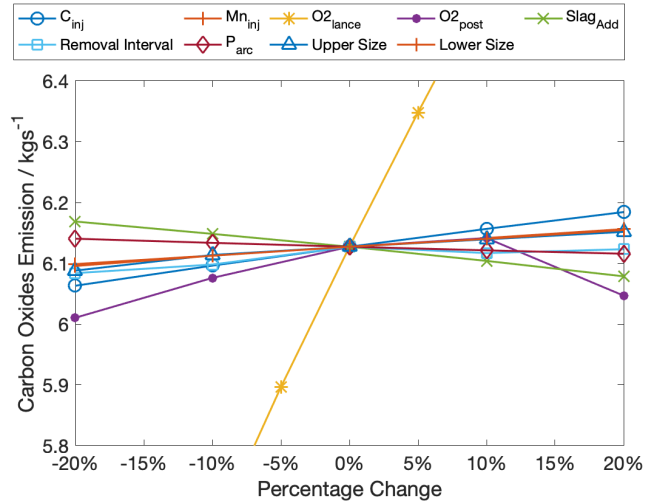
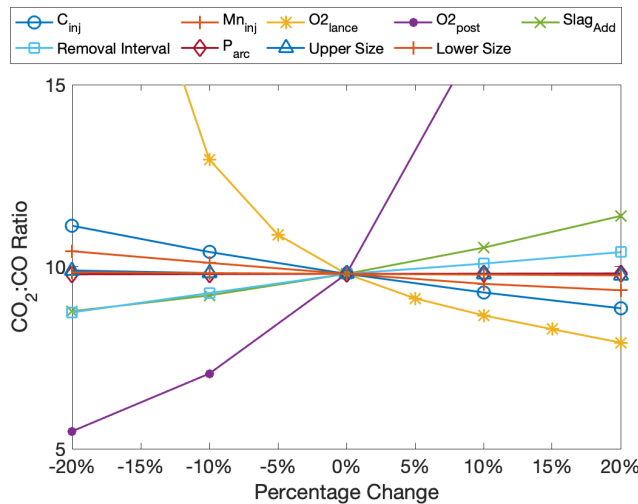

Figure 2.3.6: Sensitivity on Emission

2.3.3.6 CO$_2$:CO Ratio

Figure 2.3.7: Sensitivity on Carbon Oxides Ratio

The ratio between CO$_2$ and CO in the off-gas was chosen as one of the KPIs because CO$_2$ is a preferred means of carbon emission compared to CO due to health and safety hazards that carbon monoxide pose. From Fig. 2.3.7, it is evident that an appropriate balance between the oxygen lancing rate and oxygen post-combustion rate needs to be found in order to maintain a high ratio between CO$_2$ and CO.

Although oxygen lancing produces carbon dioxide at a rate approximately three times greater than it produces carbon monoxide, the increase in carbon monoxide still results in a a decrease of the CO$_2$:CO ratio. Therefore, the additional carbon monoxide produced via oxygen lancing needs to be mitigated with a higher oxygen post-combustion rate. In addition, the slag addition and carbon injection rates also showed a moderate linear relationship with the ratio of carbon oxides. Increasing slag addition affects the mole fraction of the metal oxides in the liquid slag, thus shifting their respective equilibria such that less decarburisation occurs and less carbon monoxide is produced. Carbon injection has the opposing effect of enhancing the decarburisation rate, resulting in more carbon monoxide present in the off-gas.

2.3.4 Optimisation

Based on results from the sensitivity analysis, the following optimisation strategy was developed:
- Due to the excess arc power in the initial model, the minimum arc power needed to melt the mixture of DRI and scrap according to their charge rate and temperature obtained from literature[9] was used. This corresponded to a value of 30 MW.

14

- Since operational inefficiency was quantified by the excess temperature greater than the melting temperature and significant iron being oxidised in the initial model, the material addition rates and arc power were optimised. For this purpose, a grid search through range of values was utilised to determine the minimised operating expenditure while meeting the composition requirement and converging to stable steady-state.
- The mechanical design heuristics of the EAF uses the EAF operating capacity to the size of furnace chamber and bath. Therefore, the upper and lower sizes of the EAF were grouped into a single parameter termed the EAF volume, which serves to represent the CAPEX expenditure.
- The removal interval was not reduced further because the current interval of 600 seconds was already short compared to the residence time of current industrial operations.
- In order to find the best mode of operation from the various options proposed at each step of the optimisation, TOPSIS was utilised as a multi-criteria decision-making method using the initial aforementioned KPIs, along with the EAF CAPEX and OPEX, which consists of the 7 different process parameters investigated using sensitivity analysis except for product removal interval and arc power. The EAF CAPEX is based on the reactor volume, which is determined by the upper chamber size and lower bath size. The EAF OPEX is determined the carbon, ferromanganese, oxygen and slag-forming input requirements.
- From a thorough trial and error analysis using results from the extensive sensitivity analysis, four sets of parameters, or 'options', were concluded to provide the best overall reactor performance. These are are described in Table 2.3.4.

Table 2.3.3: List of KPIs used for Optimisation

KPI Category	KPIs Considered
Composition Requirements	Carbon Composition, Manganese Composition
Economics	CAPEX, OPEX
Safety & Environment	Carbon Oxide Emissions, CO_2:CO Ratio
Operational Efficiency	Liquid Metal Outlet Temperature, Selectivity of Fe

Table 2.3.4: Options considered for optimisation.

	C_{inj} (kg/s)	Mn_{inj} (kg/s)	$O_{2,lance}$ (kg/s)	$O_{2,post}$ (kg/s)	Slag Addition (kg/s)	Removal Interval (s)	Arc Power (kW)	Capacity (tonnes)
Option 1	1.3	1.5	4	1	3	600	30000	200
Option 2	0.95	1.25	2.8	0.8	1.5	600	30000	200
Option 3	0.95	1.25	2.8	0.8	1.5	900	30000	220
Option 4	0.95	1.25	2.8	0.8	1.5	600	30000	180

2.3.5 Optimised EAF Reactor Model

As a result of TOPSIS analysis, Option 4 was considered to be the optimised set of operating conditions for the EAF. The details of this decision-making process can be found in Appendix 2.7.7. A visual comparison of the key differences between the initial model results and optimised model results are shown below.

Fine-tuning the various rates of material additions into the EAF proved to be a highly effective means of optimising a range of KPIs, including carbon oxide emissions, selectivity of Fe and the economic KPIs. Moreover, despite decreasing the maximum capacity and, hence, the size of the furnace, the liquid metal temperature was further decreased by limiting the combined material injections into the system in order to decrease the rates of the exothermic reactions. This effectively reduced the outlet temperature to only 130 K above the melting point of iron. Although both the initial model and optimised model met the composition requirements at the point of convergence, reducing the material addition rates improved the reliability of these outlet composition values as fluctuations were minimised and convergence to steady-state was achieved quickly.

2.3.5.1 Limitations of Optimised Model

Although the detailed reactor model provides a reasonable representation of actual EAF operation, there are inherent variabilities present due to the assumptions made in the model. For example, the model assumes complete homogeneity within each of the material zones. However, since the reactions could be

diffusion-limited, the heat liberated from the chemical reactions in the liquid metal zone could deviate from the model values. Therefore, careful monitoring and control of the EAF reactor is strongly advised.
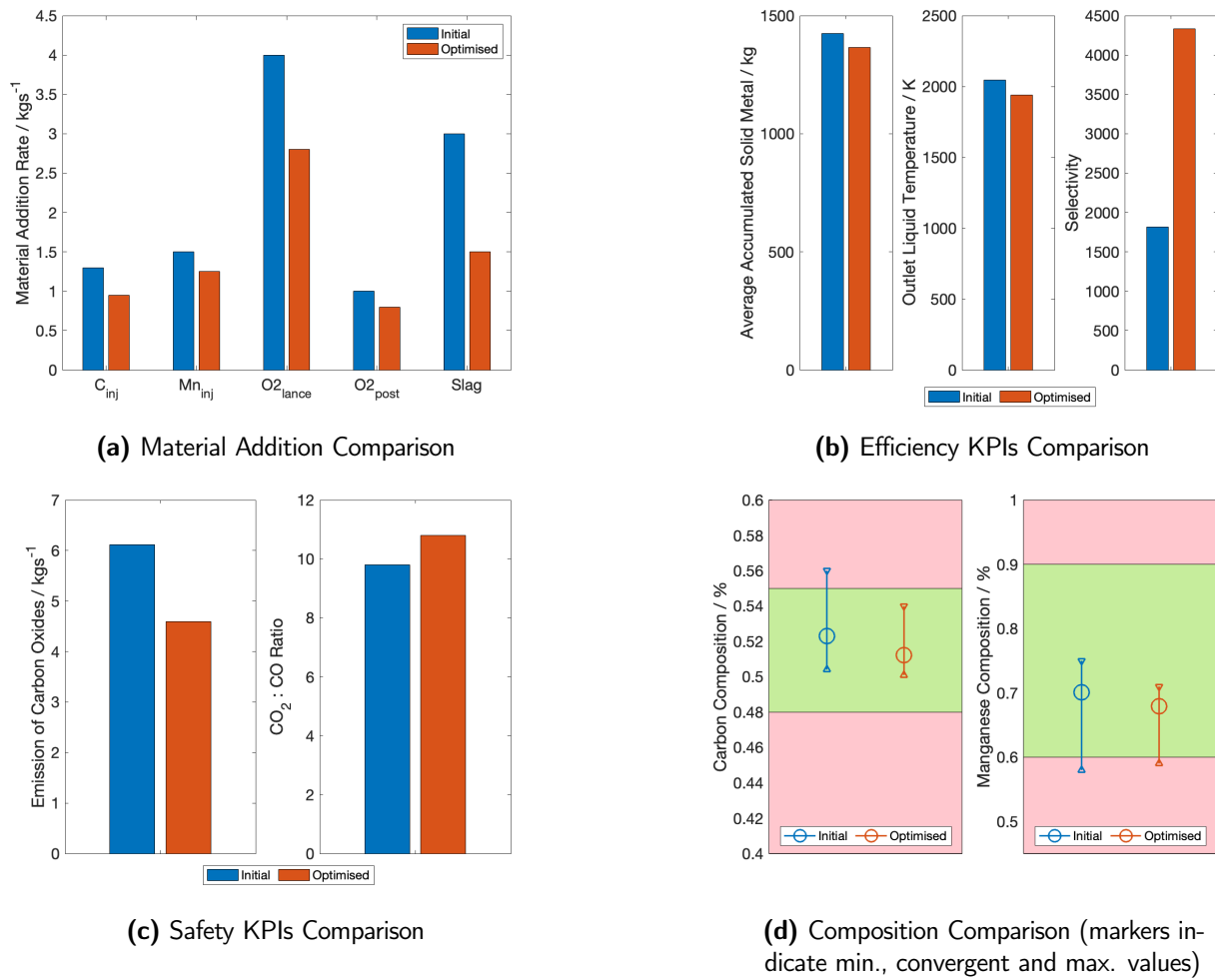

(a) Material Addition Comparison

(b) Efficiency KPIs Comparison

(c) Safety KPIs Comparison

(d) Composition Comparison (markers indicate min., convergent and max. values)

Figure 2.3.8: Comparison of Initial and Optimised Model

2.4   Mechanical Design of EAF

2.4.1   General Features

There are three major categories that incorporate the key components of an EAF - the furnace itself, the components that enable movement and the electrical system.

The hearth of EAF vessel is typically cylindrical, conical or cylindro-conical.[10] On the other hand, the shell roof and the shell bottom are usually flattened spheres. Water-cooled panels are an array of parallel tubes positioned in close proximity, placed in the upper wall region and the roof of the EAF in order to cool the furnace. The key openings that are essential to furnace operation include the electrode ports, openings for injection of oxygen and carbon, an off-gas vent, tapholes which are the outlets for liquid steel, slag doors to allow decanting of slag and an opening to continuously feed in DRI[11].

In terms of furnace movements, a batch EAF would require roof and electrode rotation or elevation to enable DRI charging, but this is not the case for a continuous EAF. However, the important movement for discharge of contents remains the same - tilting of the EAF. For bottom tapping furnaces, the tilt angle is between 15 and 20 degrees. The crucial aim is to tilt the furnace back as quickly as possible to avoid any slag entering the liquid metal in the ladle. The furnace movement is conducted using a combination of a central hydraulic system and raised support elements with wheels. The hydraulic system uses cylinders to extend and contract in order to move the furnace shell.[11]

The primary electrical component in the electrical system is the EAF transformer. The transformer receives

the primary high voltage, low current power from the grid and transforms this into a low voltage, high current power required for the arcs.[11]

2.4.2 Materials

2.4.2.1 Furnace Shell, Electrodes and Water-Cooled Panels

The furnace shell is typically made of rolled carbon steel sheets which are welded together.[10] The electrodes, on the other hand, are currently only available as graphite electrodes given it is the only material that can withstand high temperatures and efficiently transfer electrical energy.[12] Lastly, the tubes that form the water-cooled panels are usually made out of low-carbon steel.[13]

2.4.2.2 Refractory Lining

Refractory lining is important because these materials are used to prevent the high temperatures of components within the furnace from damaging the furnace shell. The refractory requirements vary between specific zones.

The hearth zone must be able to withstand corrosion when the liquid slag is tapped, and therefore typically requires two layers of refractory lining. The bottom layer is known as the safety lining, and is made up of magnesite bricks with MgO content of between 90 % to 97%, enabling it to have the slag resistance required to withstand any liquid leak through the top layer[14]. The top layer, known as the working lining, is made up of monolithic magnesite with MgO content of 60% to 95% in combination with dry granular material. This monolithic layer also contains oxide impurities such as FeO which enable sintering to take place when exposed to high temperatures, strengthening the lining.[14]

The slag line is essentially the connection between the hearth and the furnace walls. This area is primarily subjected to high temperatures from the liquid slag, and thus needs to designed based on expected slag composition. Since carbon steel is being produced rather than stainless steel, magnesite carbon bricks with C content between 10% to 20% are used for the safety lining. Monolithic magnesite is once again used for the working lining; however, these will corrode due to the operating conditions in this area. To prevent this, 'guniting' the slag line is required to build a protective layer.[14]

The side walls of the furnace are exposed to the extreme temperatures of the arc flare, flame impingement from oxygen lancing and the liquid slag that may come into contact with the walls when tapping out the liquid steel. To withstand this, high quality magnesite carbon bricks with fused magnesia grains and C content between 5% and 20% are required for the safety lining.[14]

The roof of the EAF is usually lined with alumina bricks containing Al_2O_3 content between 70% to 90% to withstand potential slag abrasion caused by the particles present in the off-gas. The increase thermal shock resistance provided by alumina is also needed to deal with the high velocity of these gases.[15]

The taphole refractory lining is positioned around the steel pipe where the taphole is located. A 450 mm diameter hole is made through the hearth refractories, where a taphole 'sleeve' made up of fused magnesia-based magnesite carbon with 10% to 15% C content[14]. The voids between the brickwork and the pipe is filled using a MgO-based guniting mix.

2.4.3 Design Aspects for Continuous Operation

The basis for design to enable continuous operation of the EAF is based on an expired patent by the Danieli Corporation.[3] The premise of design is the distinction between three separate 'melting zones' within the furnace - a central melting zone flanked with two lateral shafts that are lower in elevation than the central melting zone. Each of the two lateral shafts are equipped with a bottom tapping port that enables continuous tapping of the liquid steel, as the furnace can be tilted 15 degrees to either side to discharge the product. Each of the two lateral shafts also connect to a deslagging door in order to remove liquid slag from the furnace. The means of furnace movement is through a hydraulic actuator attached to the side of the furnace shell which can push or pull the vessel about a pivot point built around the top of the central stack. The furnace vessel is supported by bases with rollers to enable seamless movement of the vessel when tapping occurs. The central stack itself is the point of entry of the DRI and scrap steel, whereby conveyer belts will feed directly into this opening. These conveyer belts will be enclosed to prevent iron from oxidizing and to

prevent air from entering the EAF system. In terms of electrical input, results from process intensification suggested that the EAF should be powered by a turbine within a Rankine cycle heated through the energy released from a hydrogen burner within the chemical looping scheme. The power generated from the Rankine cycle is roughly double that required for the arcs in the EAF.

2.4.4   Detailed Sizing of EAF

The mechanical design of the EAF could not be based on standards provided by the British Standards Institution (BSI), as design procedures do not exist for electric arc furnaces. Traditional electric arc furnace design and sizing guidance exist in literature, and so publications by Dutta *et al.*[10] and Oyawale *et al.*[16] were used to develop furnace shell and electrode sizes. Table 2.5.1 on the next page provides the dimensions of the key components of a continuous EAF design. Where applicable, links between the mathematical model and the mechanical design are explained in order to demonstrate consistency between them. The page after Table 2.5.1 is a mechanical drawing of the final EAF. Further details can be found in Appendix 2.7.9. The water-cooled panels and hydraulic actuator have been left out due to the complexity involved. The refractory brick lining material has also been left out, as this has been discussed in detail above in Section 2.4.2.2.

2.5   Conclusion and Future Scope

Colosseum Steelworks selected the electric arc furnace (EAF) as the the reactor to be designed in detail because of its importance in the overall process, the complexity of the model and innovative nature of operation. The model proposed is based on two papers published by Logar *et al.*[1,2] as this is the most complete approach found in literature.

The model includes three major components - heat transfer, mass transfer and thermo-chemical element, all of which, when put together, represent the dynamic behaviour of the EAF. Although the paper is relatively self-contained, Colosseum Steelworks has addressed several key issues, adjusting the model to suit the purposes of company's intended process. These include the removal of methane injection to the EAF oxygen burners, the inclusion of impurities, the implementation of extensive chemical equilibrium relationships and the transformation of the batch process into a continuous process using a convergent solution to guide the steady state behaviour. In regards to assumptions, a combination of first-order ODEs and algebraic relationships were used to represent heat and mass transfer phenomena, solved using the Euler forward method. The EAF was also divided into different homogenous zones to simplify the relationships between different phases (solid, liquid and gas) present in the system. The results from model validation indicate that the model developed by Colosseum Steelworks shows reasonable agreement with the results derived from literature, whereby slight deviations can be explained by different simplifications and adjustments made.

Sensitivity analysis was conducted by exploring the effects of 9 different process parameters on six key reactor performance indicators (KPIs), which were chosen based on composition requirements, operational efficiency, economics and environmental considerations. The results of sensitivity analysis was used to optimise the EAF, yielding four sets of parameters, or 'options', that led to the best reactor performance. TOPSIS was then used to determine the best of these options, which led to improvements in all the aforementioned KPIs from the base case set of parameters.

In terms of future recommendations, Colosseum Steelworks believes that extensive research should be conducted on improving the nature of the view factor analysis included in the model. Due to the continuous mode of operation, modelling view factor behaviour such that the central melting zone and the lateral shafts are considered to be separate zones would greatly improve the reliability of results, as the radiative heat transfer phenomena would be more accurately represented. Accounting for a continuous solid metal feed with semi-continuous tapping cycles would also be a means of expanding upon the phases of operation outlined in literature. To further improve tapping times and furnace efficiency, Colosseum Steelworks will also look to adapt the findings from the patent further by testing out the viability of increasing the number of lateral shafts present within the reactor to three or four secondary zones such that tapping can occur more swiftly.

Table 2.5.1: Detailed Dimensions for EAF Design (D = Diameter, W = Width, L = Length, t = Thickness)

Description	Shape approximation	Dimensions (mm)	Justification
Furnace Shell	Conical frustum, spherical cap and cylinder	• $D_{inner} = 8168$ • $t = 50$	Step-by-step detailed furnace shell sizing using design basis by Dutta *et al.*[10] and Oyawale *et al.*[16].
Refractory Lining	-	• $t = 550$ to 600	Typical safety lining is 230 mm and the working lining is between 300 mm to 600 mm.[14] For a capacity of 100 to 200 tonnes, 600 mm is usually used.[10]
Central Electrodes	Cylinder	• $D = 400$ • $H_{total} = 5528.88$ • $H_{in-furnace} = 3328.88$ • $H_{eaf-arc} = 950$	Diameter sized using design basis by Dutta *et al.*[10] Total arc area of 4 electrodes (2 central + 2 lateral shaft) is equivalent to the arc surface area used in the mathematical model (3.58 m^2).
Lateral Shaft Electrodes	Cylinder	• $D = 200$ • $H_{total} = 4550$ • $H_{in-furnace} = 1300$ • $H_{eaf-arc} = 950$	Total arc area of 4 electrodes (2 central + 2 lateral shaft) is equivalent to the arc surface area used in the mathematical model (3.58 m^2).
O$_2$ Injection Point (Lancing)	Port	• $D_{outer} = 200$ • $D_{inner} = 135$	Retrieved from Literature[17]
Slag-forming Materials Input	Port	• $D_{outer} = 200$ • $D_{inner} = 135$	Used volumetric flowrate requirement and typical conveyer belt speed (0.33 m/s) to determine required port area.
Central stack	Cuboid	• $L = 2400$ • $W = 3000$ • $H = 2500$ • $t = 350$	Total volume sized at 10.8 m^3 to retrieve exact volume of feed every 10 min cycle (10.3 m^3).
Central melting zone	Cylindrical void	• $D = 3355.80$ • $H = 1700$	Used double of removal volume per cycle (8.4 m^3) as guideline.
Lateral shafts	Cylindrical void	• $D = 1400$ • $H = 1500$	Sized such that two lateral shafts + central melting zone volume (21 m^3) is large enough so that EAF can operate with only one tapping port if required.
Roof	Cylinder	• $D = 4000$ • $H = 1422.68$	Design basis by Dutta *et al.*.[10]
Off-gas vent	Pipe	• $D_{outer} = 1200$ • $D_{inner} = 1000$	Benchmarked with EAFs in industry.[18]
Lateral tapping ports	Port	• $D_{outer} = 200$ • $D_{inner} = 135$	Retrieved from Industry Expert.[14]
Deslagging doors	Rectangle	• $W = 1740$ • $H = 700$	Design basis by Dutta *et al.*.[10]
O$_2$ Injection Point (Post-Combustion)	Port on off-gas vent	• $D_{outer} = 200$ • $D_{inner} = 135$	Retrieved from literature.[17]

Dimensions (cross-section view, left):
- 4000.00
- 1800.00
- 350.00
- Ø 400.00
- Ø 200.00
- Ø 200.00
- 2550.00
- 1422.68
- 3328.88
- 5528.88
- 4550.00
- 950.00
- 1723.33
- 2787.00
- 700.00
- 950.00
- 1500.00
- 271.00
- 1083.00
- 1354.00
- 7808.02
- 550.00
- 600.00
- Ø 200.00
- Ø 1400.00
- 2300.00
- 1300.00
- Ø 3355.80
- 4603.00
- 6768.00
- 7526.00
- 8625.18

TITLE:
Detailed Reactor Design for Electric Arc Furnace EAF-1

DWG NO.
EAF-1

A4

SCALE:1:80   SHEET 1 OF 2

2.6   References

[1] V. Logar, D. Dovžan, and I. Škrjanc, "Modeling and Validation of an Electric Arc Furnace: Part 2, Thermo-chemistry", Tech. Rep. 3, 2012, pp. 413–423.

[2] ——, "Modeling and Validation of an Electric Arc Furnace: Part 1, Heat and Mass Transfer", *ISIJ International*, vol. 52, no. 3, pp. 402–412, 2012.

[3] Danieli Corporation and World Intellectual Property Organization, *Electric Arc Furnace for Continuous Charging*, Nov. 2000.

[4] Y. Toulouveski and I. Zinurov, *Innovation in electric arc furnaces: Scientific basis for selection*. Jan. 2010, pp. 1–258. [Online]. Available: `https://www.researchgate.net/publication/290101174_Innovation_in_electric_arc_furnaces_Scientific_basis_for_selection`.

[5] V. Logar and I. Škrjanc, "Modeling and validation of the radiative heat transfer in an electric arc furnace", *ISIJ International*, vol. 52, no. 7, pp. 1225–1232, 2012.

[6] J. B. Ian, K. Craig, and P. Christiaan, "Modeling and Simulation of an Electric Arc Furnace Process", Tech. Rep. 1, 1999, pp. 23–32.

[7] Ramesh Singh, *Applied Welding Engineering : Processes, Codes, and Standards*. Elsevier Science & Technology, Nov. 2011, pp. 1–374.

[8] METINVEST, *Steel 1050*. [Online]. Available: `https://metinvestholding.com/en/products/steel-grades/1050`.

[9] S. Hornby, J. Madias, and F. Torre, "MYTHS AND REALITIES OF CHARGING DRI/HBI IN ELECTRIC ARC FURNACES",

[10] S. K. Dutta and R. Oza, "Aspect of Design and Developments in EAF", Tech. Rep., Dec. 2014. [Online]. Available: `https://www.researchgate.net/publication/307323617`.

[11] Ispat Guru, *Design Features of an AC Electric Arc Furnace*, Feb. 2015. [Online]. Available: `https://www.ispatguru.com/design-features-of-an-ac-electric-arc-furnace/`.

[12] Coidan Graphite, *Arc Furnace Electrode*. [Online]. Available: `https://www.coidan.com/services/electrodes/arc-furnace-electrodes/#:~:text=Graphite%20electrodes%20are%20primarily%20used,is%20white%20hot%20circa%205000%C2%BAC`.

[13] D. Headquarters, "THE RELIABLE AND INNOVATIVE PARTNER IN THE METALS INDUSTRY DANIELI WATER COOLED ELEMENTS for steelmaking furnaces and equipment", Italy, Tech. Rep. [Online]. Available: `https://www.danieli.com/media/download/img_4187.pdf`.

[14] Ispat Guru, *Refractory Lining of the Electric Arc Furnace*. [Online]. Available: `https://www.ispatguru.com/refractory-lining-of-the-electric-arc-furnace/`.

[15] Elsa Gao, *Refractory materials for different parts of electric ARC furnace*, Jul. 2017. [Online]. Available: `https://www.linkedin.com/pulse/refractory-materials-different-parts-electric-arc-furnace-gao/`.

[16] D. Olawale and F. Oyawale, "Design and Prototype Development of a Mini-Electric Arc Furnace", May 2007. [Online]. Available: `https://www.researchgate.net/publication/237242189`.

[17] F. Liu, R. Zhu, G. Wei, and S. Fan, "Effect of lance structure on behavior of coherent jet in EAF steelmaking process", *Materials*, vol. 13, no. 5, Mar. 2020.

[18] M. Kirschen and H. Pfeifer, "Off-gas measurements at the EAF primary dedusting system", Tech. Rep., 2005. [Online]. Available: `https://www.researchgate.net/publication/276388593`.

[19] Zhang Y. and Fruehan R.J., "Effect Of Gas Type And Pressure On Slag Foaming", [Online]. Available: `https://link.springer.com/article/10.1007/BF02654112`.

[20] B. Bowman, J. Jones, and P. Lefrank, "Chapter 10. Electric Furnace Steelmaking", in *The Making, Shaping and Treating of Steel*, 10th ed., Pittsburgh, US: The AISE Steel Foundation, 1998, pp. 525–600.

[21] Eramet Comillog, "HIGH CARBON FERROMANGANESE HCFeMn", Tech. Rep. [Online]. Available: `www.eramet.fr%20https://www.eramet.com/sites/default/files/inline-files/eramet_high_carbon_ferromanganese_1.pdf`.

[22] E. Turkdogan, *Fundamentals of Steel Making*. Leeds: The Institute of Materials, 1996.

[23] S. Basu, A. K. Lahiri, and S. Seetharaman, "Activity of iron oxide in steelmaking slag", *Metallurgical and Materials Transactions B: Process Metallurgy and Materials Processing Science*, vol. 39, no. 3, pp. 447–456, Jun. 2008.

[24] J. G. Bekker, I. K. Craig, and P. C. Pistorius, "Modeling and Simulation of an Electric Arc Furnace Process", *ISIJ International*, vol. 39, no. 1, pp. 23–32, 1999.

[25] M. Meraikib, "Activity of Silica in the Slag of an Electric Arc Furnace Using Direct Reduced Iron for Steelmaking", Tech. Rep. 1, 1995, pp. 845–850.

[26] S. Basu, A. K. Lahiri, and S. Seetharaman, "Phosphorus partition between liquid steel and CaO-SiO2-P 2O5-MgO slag containing low FeO", *Metallurgical and Materials Transactions B: Process Metallurgy and Materials Processing Science*, vol. 38, no. 3, pp. 357–366, Jun. 2007.

2.7 Appendix

2.7.1 Detailed View Factor Equations

The detailed view factor equations incorporated in the model were obtained from Logar et al.[5].

2.7.1.1 View Factor from Arc to Roof, ($F_{Arc-Roof}$)

Theoretically, there are two obstacles that hinder the radiation from arc reaching the roof of the furnace, solid metal and electrode. Nevertheless, at the stage of convergence into the steady-state, the level of solid metal would not be as high as to interfere with the radiation of arc, thus only the disturbance of electrode should be considered.

$$F_{Arc-Roof-1} = \frac{B_1}{8RH_1} + \frac{1}{2\pi}\left(\arccos\frac{A_1}{B_1} - \frac{1}{2H_1}\left(\sqrt{\frac{(A_1+2)^2}{R^2}-4}\right)\arccos\frac{A_1 R}{B_1} - \frac{A_1}{2RH_1}\arcsin R\right)$$

$$
\begin{aligned}
R &= r_{electrode}/r_{eafout} \\
H_1 &= (h_{electrode}+h_{arc})/r_{eafout} \\
A_1 &= H_1^2 + R^2 - 1 \\
B_1 &= H_1^2 - R^2 + 1
\end{aligned}
$$
(2.59)

$$F_{Arc-Roof-2} = \frac{B_2}{8RH_2} + \frac{1}{2\pi}\left(\arccos\frac{A_2}{B_2} - \frac{1}{2H_2}\left(\sqrt{\frac{(A_2+2)^2}{R^2}-4}\right)\arccos\frac{A_2 R}{B_2} - \frac{A_2}{2RH_2}\arcsin R\right)$$

$$
\begin{aligned}
R &= r_{electrode}/r_{eafout} \\
H_1 &= h_{electrode}/r_{eafout} \\
A_1 &= H_1^2 + R^2 - 1 \\
B_1 &= H_1^2 - R^2 + 1
\end{aligned}
$$
(2.60)

$$F_{Arc-Roof} = \frac{F_{Arc-Roof-1}\cdot A_{Arc-Roof-1} - F_{Arc-Roof-2}\cdot A_{Arc-Roof-2}}{A_{Arc-Roof-3}}$$
(2.61)

2.7.1.2 View Factor from Arc to Roof ($F_{Arc-Wall}$)

The view factor of arc to wall can effectively be determined by relating to a smaller cylinder placed within bigger coaxial cylinder. The position of the arcs in relation to the wall depends on the bore-down electrode depth in the steel. The view factor can be obtained by the following equation.

$$F_{Arc-Wall} = \frac{X}{L}F_X + \frac{L-X}{L}(1-F_{L-X}) + \frac{Y+X-L}{L}F_{Y+X-L} - \frac{X+Y}{L}F_{X+Y}$$
(2.62)

where the coefficients F_X, F_{L-X}, F_{Y+X-L} and F_{X+Y} can be obtained with

$$F_\zeta = \frac{B_\zeta}{8R\zeta} + \frac{1}{2\pi}\left(\arccos\frac{A_\zeta}{B_\zeta} - \frac{1}{2\zeta}\left(\sqrt{\frac{(A_\zeta+2)^2}{R^2}-4}\right)\arccos\frac{A_\zeta R}{B_\zeta} - \frac{A_\zeta}{2R\zeta}\arcsin R\right)$$
(2.63)

where ζ equals X, L-X, Y+X-L or X+Y and they can be obtained with:

$$
\begin{aligned}
X &= h_{cone}/r_{eaf,out} \\
Y &= h_{wall}/r_{eaf,out} \\
L &= h_{arc}/r_{eaf,out} \\
R &= r_{electrode}/r_{eaf,out} \\
A_\zeta &= \zeta^2 + R^2 - 1 \\
B_\zeta &= \zeta^2 - R^2 + 1
\end{aligned}
$$
(2.64)

2.7.1.3 View Factor from Arc to Metals (F_{Arc-SM} & F_{Arc-LM})

Since the sum of view factors from a surface should sum up to unity, simple equation for view factors from the arc to the metals can be built.

$$F_{Arc-SM} = (1 - F_{Arc-Roof} - F_{Arc-Wall}) \left(1 - K_{SM-LM} \left(1 - \frac{m_{SM}}{m_{charge}} \right) \right) \tag{2.65}$$

$$F_{Arc-LM} = (1 - F_{Arc-Roof} - F_{Arc-Wall}) \left(K_{SM-LM} \left(1 - \frac{m_{SM}}{m_{charge}} \right) \right) \tag{2.66}$$

2.7.1.4 View Factor from Liquid Metal to Roof ($F_{LM-Roof}$)

$$F_{LM-Roof} = \frac{1}{2} \left(R_3^2 - R_2^2 - \sqrt{(1 + R_3^2 + H^2)^2 - 4R_3^2} + \sqrt{(1 + R_2^2 + H^2)^2 - 4R_2^2} \right)$$

$$\tag{2.67}$$

$$H = h_{wall}/r_{eaf,in}$$
$$R_2 = r_{hole}/r_{eaf,in}$$
$$R_3 = r_{eaf,out}/r_{eaf,in}$$

$$F_{Roof-LM} = F_{LM-Roof} \frac{A_{LM}}{A_{Roof}} \tag{2.68}$$

2.7.1.5 View Factor from Roof to Solid Metal ($F_{Roof-SM}$)

In the continuous operation, due to small volume of solid metal in steady-state, the radiative surface of solid metal is approximated by the curved surface of cone frustum.

$$F_{Roof-SM} = \frac{2R^2 - X + \sqrt{X^2 - 4R^2}}{2\sqrt{X - 2R} \cdot (1 + R)} \cdot F_{LM-Roof}$$

$$\tag{2.69}$$

$$H = h_{cone}/r_{cone,in}$$
$$R = r_{cone,out}/r_{cone,in}$$
$$X = 1 + R^2 + H^2$$

Then, the inverse view factor can be found as well:

$$F_{SM-Roof} = F_{Roof-SM} \frac{A_{Roof}}{A_{SM}} \tag{2.70}$$

2.7.1.6 View Factor from Solid Metal to Wall ($F_{SM-Wall}$)

$$F_{SM-Wall} = \frac{1}{2} \left(1 + \frac{1}{R^2 - 1} \left[H\sqrt{4R^2 + H^2} - \sqrt{(1 + R^2 + H^2)^2 - 4R^2} \right] \right)$$

$$\tag{2.71}$$

$$H = h_{wall}/r_{cone,out}$$
$$R = r_{eaf,out}/r_{cone,out}$$

$$F_{Wall-SM} = F_{SM-Wall} \frac{A_{SM}}{A_{Wall}} \tag{2.72}$$

2.7.1.7 View Factor from Liquid Metal to Wall ($F_{LM-Wall}$)

$$F_{LM-Wall} = \frac{1}{2} \left(1 - R^2 + H^2 + \sqrt{(1 + R^2 + H^2)^2 - 4R^2} \right)$$

$$\tag{2.73}$$

$$H = h_{wall}/r_{eaf,in}$$
$$R = r_{eaf,out}/r_{eaf,in}$$

$$F_{Wall-LM} = F_{LM-Wall} \frac{A_{LM}}{A_{Wall}} \tag{2.74}$$

2.7.2 Slag Foaming Model

Slag foaming in modern practice is an important aspect to be considered as appropriate degree of slag foaming contributes towards energy efficiency by both protecting radiative heat loss to the roof and wall and by reducing the impedance load of slag from stabilising the arc burning.

According to Zhang and Fruhan, 1995,[19] the change of slag height due to slag foaming could be determined by the slag-foaming index(Ξ) and the superficial gas velocity.

$$H_f = \Xi U_g \tag{2.75}$$

Where the slag-foaming index could be obtained by rheological properties of slag such as viscosity(ν), surface tension(σ) and density(ρ). The values for these properties could be approximated from the graph presented in the literature (Fruhan & Turkdogan, 1999).

$$\Xi = \frac{115\nu^{1.2}}{\sigma^{0.2}\rho D_B^{0.9}} \tag{2.76}$$

The bubble diameter can be obtained by the following equations:

$$D_B = \left(\frac{3}{C_d \rho_g \rho_l^2}\right)^{\frac{1}{3}} \frac{2\sigma}{U_B^2} \tag{2.77}$$

Then, the superficial gas velocity can be approximated by the following equation, where dm_{CO} is the rate of mass change of carbon monoxide, R is the universal gas constant and $P_g as$ is the pressure of the gas zone.

$$U_g = \frac{dm_{CO} R T_{gas}}{P_{gas} A_{bath}} \tag{2.78}$$

Finally, the effect of slag foaming is calculated by the following correlation proposed by MacRosty, 2005.

$$K_{slag} = 0.7\left(\frac{1}{2}\tanh 5 H_f - 1.25 + \frac{1}{2}\right)\left(\frac{1}{2}\tanh 3.2\left(1 - \frac{m_{sSc}}{m_{max}}\right) - 1.29 + \frac{1}{2}\right) \tag{2.79}$$

Then the view factors $F_{Arc-Roof}$ and $F_{Arc-Wall}$ are multiplied by $(1 - K_{slag})$ in order to apply the protective effect of slag foaming from the radiative heat transfer of liquid metal and slag.

2.7.3 Electrode Consumption Model

Since the electrodes in EAF are made up of graphite, it goes under oxidation reaction with oxygen present in the gas zone to produce carbon dioxide. Therefore, it is important to keep track of electrode consumption in order to keep track of carbon dioxide produced and to estimate the relevant economic parameters. The model proposed by Bowman, 1998[20] was used to describe the electrode consumption ($\dot{m}_{el}$)

$$\dot{m}_{el} = 3\left(R_{tip}\frac{I_{arc}^2}{3600} + R_{side}\frac{A_{side}}{3600}\right) \tag{2.80}$$

where R_{tip} and R_{side} are the average oxidation rates for electrode tip and side, I_{arc} is the arc current and A_{side} is the electrode side surface area.

2.7.4 Mass Addition Compositions

Table 2.7.1: Composition of Solid Scrap[1]

C	Si	Cr	P	Mn	C_9H_{20}
0.4%	0.6%	0.2%	0.05%	0.6%	1.1%

Table 2.7.2: Composition of Slag-forming Material[6]

CaO	MgO	SiO_2	Al_2O_3
56.7%	41.2%	0.7%	0.45%

Table 2.7.3: Composition of Ferromanganese[21]

Mn	Fe	C	Si	P
78%	14.5%	7%	0.3%	0.2%

2.7.4.1 Enthalpies of Reaction

The individual enthalpies of reaction for each reaction **(a)** to **(n)** in Section 2.2.4.1 are listed below, with the subscript of the enthalpy representing each specific reaction. The specific heat capacity terms our functions of temperature, of which correlations were obtained from NIST.

$$\Delta H^{\circ}_{T-\textbf{(a)}} = \frac{\dot{m}_{Fe,3}}{M_{Fe}}\left((\Delta H_{FeO} - \Delta H_{Fe-S}) + \int_{298}^{T_{LM}}\left(C_{p,FeO} - C_{p,Fe} - 0.5C_{p,O_2}\right)dT\right) \tag{2.81}$$

$$\Delta H^{\circ}_{T-\textbf{(b)}} = \frac{\dot{m}_{C-L,2} + \dot{m}_{C-D,1}}{M_C}\left((\Delta H_{CO} - \Delta H_{C-S} - \Delta H_{FeO}) + \int_{298}^{T_{LM}}\left(C_{p,Fe} + C_{p,CO} - C_{p,C} - C_{p,FeO}\right)dT\right) \tag{2.82}$$

$$\Delta H^{\circ}_{T-\textbf{(c)}} = \frac{\dot{m}_{Mn,1}}{M_{Mn}}\left((\Delta H_{MnO} - \Delta H_{FeO} - \Delta H_{Mn-S}) + \int_{298}^{T_{LM}}\left(C_{p,Fe} + C_{p,MnO} - C_{p,FeO} - C_{p,Mn}\right)dT\right) \tag{2.83}$$

$$\Delta H^{\circ}_{T-\textbf{(d)}} = \frac{\dot{m}_{Si,1}}{M_{Si}}\left((\Delta H_{SiO_2} + \Delta H_{SiO_2-S} - 2\Delta H_{FeO} - \Delta H_{Si-S}) + \int_{298}^{T_{LM}}\left(2C_{p,Fe} + C_{p,SiO_2} - 2C_{p,FeO} - C_{p,Si}\right)dT\right) \tag{2.84}$$

$$\Delta H^{\circ}_{T-\textbf{(e)}} = \frac{\dot{m}_{Cr,1}}{M_{Cr}}\left((\Delta H_{Cr_2O_3} - 3\Delta H_{FeO} - 2\Delta H_{Cr-S}) + \int_{298}^{T_{LM}}\left(3C_{p,Fe} + C_{p,Cr_2O_3} - 3C_{p,FeO} - 2C_{p,Cr}\right)dT\right) \tag{2.85}$$

$$\Delta H^{\circ}_{T-\textbf{(f)}} = \frac{\dot{m}_P}{M_P}\left((\Delta H_{P_2O_5} - 5\Delta H_{FeO} - 2\Delta H_{P-S}) + \int_{298}^{T_{LM}}\left(5C_{p,Fe} + C_{p,P_2O_5} - 5C_{p,FeO} - 2C_{p,P}\right)dT\right) \tag{2.86}$$

$$\Delta H^{\circ}_{T-\textbf{(g)}} = \frac{\dot{m}_{C-D,2}}{M_C}\left((\Delta H_{CO} - \Delta H_{C-S}) + \int_{298}^{T_{LM}}\left(C_{p,CO} - C_{p,C} - 0.5C_{p,O_2}\right)dT\right) \tag{2.87}$$

$$\Delta H^{\circ}_{T-\textbf{(h)}} = \frac{O_{2,Post} \cdot K_{mCO}}{M_{O_2}}\left((\Delta H_{CO_2} - \Delta H_{CO}) + \int_{298}^{T_{Gas}}\left(C_{p,CO_2} - C_{p,CO} - 0.5C_{p,O_2}\right)dT\right) \tag{2.88}$$

$$\Delta H^{\circ}_{T-\textbf{(i)}} = \frac{\dot{m}_{C-D,5}}{M_C}\left((\Delta H_{CO_2} - \Delta H_{C-S}) + \int_{298}^{T_{LM}}\left(C_{p,CO_2} - C_{p,C} - C_{p,O_2}\right)dT\right) \tag{2.89}$$

$$\Delta H^{\circ}_{T-\textbf{(j)}} = -\frac{\dot{m}_{Mn,2}}{M_{Mn}}\left((\Delta H_{CO} + \Delta H_{Mn-S} - \Delta H_{MnO} - \Delta H_{C-S}) + \int_{298}^{T_{LM}}\left(C_{p,Mn} + C_{p,CO} - C_{p,MnO} - C_{p,C}\right)dT\right) \tag{2.90}$$

$$\Delta H^{\circ}_{T-\textbf{(k)}} = \frac{\dot{m}_{Si,3}}{M_{Si}}\left((\Delta H_{SiO_2} + \Delta H_{SiO_2-S} + 2\Delta H_{Mn-S} - 2\Delta H_{MnO} - \Delta H_{Si-S})\right.$$
$$\left. + \int_{298}^{T_{LM}}\left(2C_{p,Mn} + C_{p,SiO_2} - 2C_{p,MnO} - C_{p,Si}\right)dT\right) \tag{2.91}$$

$$\Delta H^{\circ}_{T-\textbf{(l)}} = \frac{\dot{m}_{Si,2}}{M_{Si}}\left((\Delta H_{SiO_2} + \Delta H_{SiO_2-S} - \Delta H_{Si-S}) + \int_{298}^{T_{LM}}\left(C_{p,SiO_2} - C_{p,Si} - C_{p,O_2}\right)dT\right) \tag{2.92}$$

$$\Delta H^{\circ}_{T-\textbf{(m)}} = \frac{\dot{m}_{Cr,2}}{M_{Cr}}\left((\Delta H_{Cr_2O_3} - 2\Delta H_{Cr-S}) + \int_{298}^{T_{LM}}\left(C_{p,Cr_2O_3} - 2C_{p,Cr} - 1.5C_{p,O_2}\right)dT\right) \tag{2.93}$$

$$\Delta H^{\circ}_{T-\textbf{(n)}} = -\frac{\dot{m}_{comb}}{M_{C_9H_{20}}}\left((9\Delta H_{CO_2} + 10\Delta H_{H_2O} - \Delta H_{C_9H_{20}}) + \int_{298}^{T_{Gas}}\left(9C_{p,CO_2} + 10C_{p,H_2O} - C_{p,C_9H_{20}} - 14C_{p,O_2}\right)dT\right) \tag{2.94}$$

2.7.5 Reaction Rates

The reaction rates for each of the components in the EAF thermo-chemical model are listed below[1].

Table 2.7.4: Rate of change of injected C ($\dot{m}_{C-L}$)

Carbon (C) Rate Change Component	Carbon (C) Rate Change Component Equation
C Injection ($\dot{m}_{C-L,1}$)	$\dot{m}_{C-L,1} = C_{inj}$
Reaction (**b**): Injected C Decarburization ($\dot{m}_{C-L,2}$)	$\dot{m}_{C-L,2} = -\dfrac{m_{FeO} \cdot r_{C-L} \cdot m_{C-L}}{m_{LSl} + m_{FeO} + m_{SiO_2} + m_{MnO} + m_{Cr_2O_3} + m_{P_2O_5}}$
Dissolution of Injected C ($\dot{m}_{C-L,3}$)	$\dot{m}_{C-L,3} = -\dfrac{m_{C-L} \cdot T_{LM} \cdot C_{p,LM} \cdot \frac{T_{Air}}{T_{Melt}}}{\lambda_C + C_{p,C} \cdot (T_{Melt} - T_{Air})}$
$\dot{m}_{C-L} = \sum_{i=1}^{3} \dot{m}_{C-L,i}$	

Table 2.7.5: Rate of change of dissolved C in liquid metal ($\dot{m}_{C-D}$)

Carbon (C) Rate Change Component	Carbon (C) Rate Change Component Equation
Reaction (**b**): Dissolved C Decarburization ($\dot{m}_{C-D,1}$)	$\dot{m}_{C-D,1} = -r_{C-D} \cdot (x_C - x_C^{eq})$
Reaction (**g**): C Oxidation to CO ($\dot{m}_{C-D,2}$)	$\dot{m}_{C-D,2} = -r_{C-1} \cdot (x_C - x_C^{eq}) \cdot O_{2,Lance} \cdot K_{O_2-CO}$
Dissolution of Injected C ($\dot{m}_{C-D,3}$)	$\dot{m}_{C-D,3} = -\dot{m}_{C-L,3}$
Reaction (**j**): MnO Decarburization ($\dot{m}_{C-D,4}$)	$\dot{m}_{C-D,4} = -r_{Mn-1} \cdot \dfrac{M_C}{M_{MnO}} \cdot (x_{MnO} - x_{MnO-1}^{eq})$
Reaction (**i**): C Oxidation to CO_2 ($\dot{m}_{C-D,5}$)	$\dot{m}_{C-D,5} = -r_{C-2} \cdot (x_C - x_C^{eq}) \cdot O_{2,Lance} \cdot K_{O_2-CO_2}$
$\dot{m}_{C-D} = \sum_{i=1}^{5} \dot{m}_{C-D,i}$	

Table 2.7.6: Rate of change of dissolved Si in liquid metal ($\dot{m}_{Si}$)

Silicon (Si) Rate Change Component	Silicon (Si) Rate Change Component Equation
Reaction (**d**): Si Desiliconization ($\dot{m}_{Si,1}$)	$\dot{m}_{Si,1} = -r_{Si-1} \cdot (x_{Si} - x_{Si}^{eq})$
Reaction (**l**): Si Oxidation to SiO_2 ($\dot{m}_{Si,2}$)	$\dot{m}_{Si,2} = -r_{Si-2} \cdot (x_{Si} - x_{Si}^{eq}) \cdot O_{2,Lance} \cdot K_{O_2-SiO_2}$
Reaction (**k**): Si with MnO ($\dot{m}_{Si,3}$)	$\dot{m}_{Si,3} = -r_{Mn-2} \dfrac{M_{Si}}{M_{MnO}} \cdot (x_{MnO} - x_{MnO-2}^{eq})$
$\dot{m}_{Si} = \sum_{i=1}^{3} \dot{m}_{Si,i}$	

Table 2.7.7: Rate of change of dissolved Mn in liquid metal ($\dot{m}_{Mn}$)

Manganese (Mn) Rate Change Component	Manganese (Mn) Rate Change Component Equation
Reaction (**c**): Mn with FeO ($\dot{m}_{Mn,1}$)	$\dot{m}_{Mn,1} = -r_{Mn} \cdot (x_{Mn} - x_{Mn}^{eq})$
Reaction (**j**): MnO with C ($\dot{m}_{Mn,2}$)	$\dot{m}_{Mn,2} = -\dfrac{M_{Mn}}{M_C} \cdot \dot{m}_{C-D,4}$
Reaction (**k**): MnO with Si ($\dot{m}_{Mn,3}$)	$\dot{m}_{Mn,3} = -\dfrac{M_{Mn}}{M_{Si}} \cdot \dot{m}_{Si,3}$
$\dot{m}_{Mn} = \sum_{i=1}^{3} \dot{m}_{Mn,i}$	

Table 2.7.8: Rate of change of dissolved Cr in liquid metal ($\dot{m}_{Cr}$)

Chromium (Cr) Rate Change Component	Chromium (Cr) Rate Change Component Equation
Reaction (**e**): Cr with FeO ($\dot{m}_{Cr,1}$)	$\dot{m}_{Cr,1} = -2r_{Cr-1} \cdot (x_{Cr} - x_{Cr}^{eq})$
Reaction (**m**): Cr Oxidation ($\dot{m}_{Cr,2}$)	Reaction (**m**): $\dot{m}_{Cr,2} = -2r_{Cr-2} \cdot (x_{Cr} - x_{Cr}^{eq}) \cdot O_{2,Lance} \cdot K_{O_2-Cr_2O_3}$
$\dot{m}_{Cr} = \sum_{i=1}^{2} \dot{m}_{Cr,i}$	

Table 2.7.9: Rate of change of dissolved P in liquid metal ($\dot{m}_P$)

Phosphorus (P) Rate Change	Phosphorus (P) Rate Change Equation
P Oxidation ($\dot{m}_P$)	$\dot{m}_P = -2r_P \cdot (x_P - x_P^{eq})$

Table 2.7.10: Rate of change of FeO in liquid slag ($\dot{m}_{FeO}$)

Iron Oxide (FeO) Rate Change Component	Iron Oxide (FeO) Rate Change Component Equation
Reaction **(b)**: Injected C Decarburization ($\dot{m}_{FeO,1}$)	$\dot{m}_{FeO,1} = \frac{M_{FeO}}{M_C} \cdot \dot{m}_{C-L,2}$
Reaction **(d)**: Si Desiliconization ($\dot{m}_{FeO,2}$)	$\dot{m}_{FeO,2} = 2\frac{M_{FeO}}{M_{Si}} \cdot \dot{m}_{Si,1}$
Reaction **(a)**: Fe Oxidation ($\dot{m}_{FeO,3}$)	$\dot{m}_{FeO,3} = 2\frac{M_{FeO}}{M_{O_2}} \cdot O_{2,Lance} \cdot K_{O_2-FeO}$
Reaction **(b)**: Dissolved C Decarburization ($\dot{m}_{FeO,4}$)	$\dot{m}_{FeO,4} = \frac{M_{FeO}}{M_C} \cdot \dot{m}_{C-D,1}$
Reaction **(e)**: Cr with FeO ($\dot{m}_{FeO,5}$)	$\dot{m}_{FeO,5} = 1.5\frac{M_{FeO}}{M_{Cr}} \cdot \dot{m}_{Cr,1}$
Reaction **(c)**: Mn with FeO ($\dot{m}_{FeO,6}$)	$\dot{m}_{FeO,6} = \frac{M_{FeO}}{M_{Mn}} \cdot \dot{m}_{Mn,1}$
Reaction **(f)**: P Oxidation ($\dot{m}_{FeO,7}$)	$\dot{m}_{FeO,7} = 2.5\frac{M_{FeO}}{M_P} \cdot \dot{m}_P$
$\dot{m}_{FeO} = \sum_{i=1}^{7} \dot{m}_{FeO,i}$	

Table 2.7.11: Rate of change of SiO$_2$ in liquid slag ($\dot{m}_{SiO_2}$)

Silicon Oxide (SiO$_2$) Rate Change Equation
Reactions **(d)**, **(k)** and **(l)**: $\dot{m}_{SiO_2} = -\frac{M_{SiO_2}}{M_{Si}} \cdot \dot{m}_{Si}$

Table 2.7.12: Rate of change of MnO in liquid slag ($\dot{m}_{MnO}$)

Manganese Oxide (MnO) Rate Change Equation
Reactions **(c)**, **(j)** and **(k)**: $\dot{m}_{MnO} = -\frac{M_{MnO}}{M_{Mn}} \cdot \dot{m}_{Mn}$

Table 2.7.13: Rate of change of Cr$_2$O$_3$ in liquid slag ($\dot{m}_{Cr_2O_3}$)

Chromium Oxide (Cr$_2$O$_3$) Rate Change Equation
Reactions **(e)** and **(m)**: $\dot{m}_{Cr_2O_3} = -\frac{M_{Cr_2O_3}}{2M_{Cr}} \cdot \dot{m}_{Cr}$

Table 2.7.14: Rate of change of P$_2$O$_5$ in liquid slag ($\dot{m}_{P_2O_5}$)

Phosphorus Oxide (P$_2$O$_5$) Rate Change Equation
$\dot{m}_{P_2O_5} = -\frac{M_{P_2O_5}}{2M_P} \cdot \dot{m}_P$

Table 2.7.15: Rate of change of Fe in liquid metal ($\dot{m}_{Fe}$)

Iron (Fe) Rate Change Component	Iron (Fe) Rate Change Component Equation
Reaction **(b)**: Injected C Decarburization ($\dot{m}_{Fe,1}$)	$\dot{m}_{Fe,1} = -\frac{M_{Fe}}{M_C} \cdot \dot{m}_{C-L,2}$
Reaction **(d)**: Si Desiliconization ($\dot{m}_{Fe,2}$)	$\dot{m}_{Fe,2} = -2\frac{M_{Fe}}{M_{Si}} \cdot \dot{m}_{Si,1}$
Fe Oxidation ($\dot{m}_{Fe,3}$)	$\dot{m}_{Fe,3} = -\frac{M_{Fe}}{M_{FeO}} \cdot \dot{m}_{FeO,3}$
Reaction **(b)**: Dissolved C Decarburization ($\dot{m}_{Fe,4}$)	$\dot{m}_{Fe,4} = -\frac{M_{Fe}}{M_C} \cdot \dot{m}_{C-D,1}$
Reaction **(e)**: Cr with Fe ($\dot{m}_{Fe,5}$)	$\dot{m}_{Fe,5} = -1.5\frac{M_{Fe}}{M_{Cr}} \cdot \dot{m}_{Cr,1}$
Mn with FeO ($\dot{m}_{Fe,6}$)	$\dot{m}_{Fe,6} = -\frac{M_{Fe}}{M_{Mn}} \cdot \dot{m}_{Mn,1}$
P Oxidation ($\dot{m}_{Fe,7}$)	$\dot{m}_{Fe,7} = -2.5\frac{M_{Fe}}{M_P} \cdot \dot{m}_P$
$\dot{m}_{Fe} = \sum_{i=1}^{7} \dot{m}_{Fe,i}$	

Table 2.7.16: Rate of change of CO in the gas ($\dot{m}_{CO}$)

Carbon Monoxide (CO) Rate Change Component	Carbon Monoxide (CO) Rate Change Component Equation
CO Extraction Through Off-gas Vents ($\dot{m}_{CO,1}$)	$\dot{m}_{CO,1} = -\frac{h_d \cdot u_1 \cdot m_{CO}}{(k_U u_2 + h_d) \cdot (m_{CO} + m_{CO_2} + m_{N_2} + m_{O_2})}$
Reactions **(b)**, **(g)** and **(j)**: C Oxidation to CO ($\dot{m}_{CO,2}$)	$\dot{m}_{CO,2} = -\frac{M_{CO}}{M_C} \cdot (\dot{m}_{C-L,2} + \dot{m}_{C-D,1} + \dot{m}_{C-D,2} + \dot{m}_{C-D,4})$
CO Post Combustion ($\dot{m}_{CO,3}$)	$\dot{m}_{CO,3} = -2\frac{M_{CO}}{M_{O_2}} \cdot O_{2,Post} \cdot K_{mCO}$
If $r_P > 0$	$\dot{m}_{CO} = \sum_{i=1}^{3} \dot{m}_{CO,i} - \dot{m}_{CO,3}$
If $r_P < 0$	$\dot{m}_{CO} = \sum_{i=1}^{3} \dot{m}_{CO,i}$

Table 2.7.17: Rate of change of CO_2 in the gas ($\dot{m}_{CO_2}$)

Carbon Dioxide (CO_2) Rate Change Component	Carbon Dioxide (CO_2) Rate Change Component Equation
CO_2 Extraction Through Off-gas Vents ($\dot{m}_{CO_2,1}$)	$\dot{m}_{CO_2,1} = -\dfrac{h_d \cdot u_1 \cdot m_{CO_2}}{(k_U u_2 + h_d) \cdot (m_{CO} + m_{CO_2} + m_{N_2} + m_{O_2})}$
CO Post Combustion ($\dot{m}_{CO_2,2}$)	$\dot{m}_{CO_2,2} = -2\dfrac{M_{CO_2}}{M_{O_2}} \cdot O_{2,Post} \cdot K_{mCO}$
C_9H_{20} Oxidation ($\dot{m}_{CO_2,4}$)	$\dot{m}_{CO_2,4} = -9\dfrac{M_{CO_2}}{M_{C_9H_{20}}} \dot{m}_{comb}$
Reaction **(i)**: C Oxidation to CO_2 ($\dot{m}_{CO_2,5}$)	$\dot{m}_{CO_2,5} = -\dfrac{M_{CO_2}}{M_C} \cdot \dot{m}_{C-D,5}$
Electrode Consumption ($\dot{m}_{CO_2,6}$)	$\dot{m}_{CO_2,6} = \dot{m}_{el}$
$\dot{m}_{CO_2} = \sum_{i=1}^{6} \dot{m}_{CO_2,i}$	

Table 2.7.18: Rate of change of O_2 in the gas ($\dot{m}_{O_2}$)

Oxygen (O_2) Rate Change Component	Oxygen (O_2) Rate Change Component Equation
O_2 Extraction Through Off-gas Vents ($\dot{m}_{O_2,1}$)	$\dot{m}_{O_2,1} = -\dfrac{h_d \cdot u_1 \cdot m_{O_2}}{(k_U u_2 + h_d) \cdot (m_{CO} + m_{CO_2} + m_{N_2} + m_{O_2})}$
Reactions **(b)**, **(g)**: C Oxidation to CO ($\dot{m}_{CO,2}$)	$\dot{m}_{CO,2} = -\dfrac{M_{CO}}{M_C} \cdot (\dot{m}_{C-L,2} + \dot{m}_{C-D,1} + \dot{m}_{C-D,2} + \dot{m}_{C-D,4})$
Reactions **(b)**, **(g)**: C Oxidation to CO_2 ($\dot{m}_{CO_2,2}$)	$\dot{m}_{CO,2} = -\dfrac{M_{CO}}{M_C} \cdot (\dot{m}_{C-L,2} + \dot{m}_{C-D,1} + \dot{m}_{C-D,2} + \dot{m}_{C-D,4})$
CO Post Combustion ($\dot{m}_{O_2,2}$)	$\dot{m}_{O_2,2} = O_{2,Post} \cdot (1 - K_{mCO})$
C_9H_{20} Oxidation ($\dot{m}_{O_2,3}$)	$\dot{m}_{O_2,3} = -14\dfrac{M_{O_2}}{M_{C_9H_{20}}} \dot{m}_{comb}$
Fe Oxidation ($\dot{m}_{O_2,4}$)	$\dot{m}_{O_2,4} = -\dfrac{M_{O_2}}{M_{FeO}} \cdot \dot{m}_{FeO,3}$
Electrode Consumption ($\dot{m}_{O_2,5}$)	$\dot{m}_{O_2,5} = -\dot{m}_{el}$
$\dot{m}_{O_2} = \sum_{i=1}^{5} \dot{m}_{O_2,i}$	

Table 2.7.19: Rate of change of C_9H_{20} in liquid metal ($\dot{m}_{comb}$)

Combustibles (C_9H_{20}) Rate Change Equation - Combustion
$\dot{m}_{comb} = -r_{comb} \cdot m_{comb} \cdot \dfrac{T_{SM}}{T_{Melt}}$

2.7.6 Thermodynamic Equilibriums

2.7.6.1 Thermodynamic Activity

Thermodynamic equilibrium was examined in detail in order to determine accurate value of equilibrium molar fraction of components at each time segment of operation, as the thermodynamic equilibrium in slag varies with various phisicochemical properties of slag mixture, such as basicity, mole fraction of component, temperature, etc. Since the resultant slag mixture mainly consists of FeO, MgO, CaO, SiO_2 and Al_2O_3, quaternary or ternary system of these compounds were appropriately assumed in ascertaining the properties of slag mixture.

Let us consider the following chemical reaction forming equilibrium at constant temperature and pressure.

$$aA + bB \rightarrow cC + dD \tag{2.95}$$

Then, the equilibrium constant of the reaction can be described using the activities of the reactants and the products.

$$K = \frac{(a_A)^a (a_B)^b}{(a_C)^c (a_D)^d} \tag{2.96}$$

The equilibrium constant can also be derived by the standard free energy.

$$\Delta G^\circ = -RT \ln K \tag{2.97}$$

Then, equilibrium constant can be computed in the function of temperature only as ΔG° is function of temperature. By rearranging and substituting log for ln:

$$\log K = -\frac{\Delta G^\circ}{19.144T} \tag{2.98}$$

For many of the activity calculation, Henry's law, which states that the activity is proportional to the activity in infinitely dilute solution, was assumed. This tends to be a fair assumption in our system, as most of impurities are present in negligible mole fractions.

$$a_i = \gamma_i N_i \tag{2.99}$$

2.7.6.2 Equilibrium Molar Fraction of Carbon (C)

For the oxidation of carbon, the equilibrium relation could be defined as (Turkdogan, 1996, eqn 6.5a)[22]:

$$K_{FC} = \frac{p_{CO}}{[\%C]a_{FeO}} \tag{2.100}$$

Where the equilibrium constant K_{FC} can be defined by (Turkdogan, 1996, eqn 6.5b)[22]:

$$\log K_{FC} = -\frac{5730}{T} + 5.096 \tag{2.101}$$

The activity of FeO was obtained using activity coefficient relationship researched by Basu et al., 2008 $(r^2 = 0.89)$[23]:

$$\log \gamma_{FeO} = \frac{1262}{T_{ISc}} - 1.1302 X_{FeO} + 0.96 X_{SiO_2} + 0.123 X_{CaO} - 0.4198 \tag{2.102}$$

Therefore, the equilibrium concentration constant for the reaction can be defined by (Turkdogan, 1996, eqn 6.6)[22]:

$$k_{C\%} = (\%FeO)[\%C] = \frac{p_{CO}}{K_{FC}\left(\frac{\gamma_{FeO}}{1.65 \cdot M_{FeO}}\right)} \tag{2.103}$$

The concentration constant can now be transformed as the product of mole fractions:

$$k_{XC} = X_{FeO} X_C = k_{C\%}\left(\frac{M_{ISI} M_{Fe}}{M_{FeO} M_C 100^2}\right) \tag{2.104}$$

Finally, the equilibrium molar fraction of carbon X_C^{eq} can be determined by following equation (Bekker, 1999, eqn 9)[24]:

$$X_C^{eq} = k_{XC}\left(\frac{m_{ISI} M_{FeO}}{m_{FeO} M_{ISI}} + \frac{m_{SiO_2} M_{FeO}}{m_{FeO} M_{SiO_2}} + 1\right) \tag{2.105}$$

2.7.6.3 Equilibrium Mole Fraction of MnO in decarburization (MnO)

The relationship of equilibrium constant and the equilibrium mole fraction was obtained from (Logar, 2012)[1]

$$kX_{Mn-1} = 6.4 p_{CO} X_{MnO} \tag{2.106}$$

$$X_{MnO-1}^{eq} = \frac{X_{Mn}}{kX_{Mn1}} \tag{2.107}$$

2.7.6.4 Equilibrium Mole Fraction of Silicon (Si)

The equilibrium equation for the oxidation of silicon can be described by (Turkdogan, 1996, eqn 6.9a)[22]:

$$K_{Si} = \frac{a_{SiO_2}}{[\%Si][\%O]^2} \tag{2.108}$$

The equilibrium constant of the reaction can be obtained by:

$$\log K_{Si} = \frac{30410}{T_{ISc}} - 11.59 \tag{2.109}$$

Due to the amount of silica content flowing from the DRI upstream, the amount of silica in slag is not negligible. Therefore, naive approach of approximating activity of silica using Henry's law is not appropriate. Instead, the activity of silica was obtained from the empirical relationship with basicity and temprature of the slag (Meraikib, 1995)[25].

$$\ln a_{SiO_2} = \frac{6728}{T_{ISI}} - (0.920B + 6.994) \tag{2.110}$$

where basicity B can be described by:

$$B = \frac{MX_{CaO} MX_{MgO}}{MX_{SiO_2} MX_{Al_2O_3}} \tag{2.111}$$

The solubility of the oxygen is determined from (Turkdogan, 1996, eqn 4.34)[22]:

$$\log[\%O] = -\frac{6380}{T_{ISc}} + 2.765 \tag{2.112}$$

Then the Equilibrium molar fraction of Silicon can be determined by converting the mass percentage of silicon:

$$X_{Si}^{eq} = [\%Si]\left(\frac{M_{Fe}}{100 \cdot M_{Si}}\right) \tag{2.113}$$

2.7.6.5 Equilibrium Mole Fraction of MnO in Reaction with Silicon (MnO)

As described in (Logar, 2012, eqn 14)[1], the equilibrium molar fraction of MnO with Si can effectively be found by the following equation:

$$X_{MnO-2}^{eq} = \sqrt{\frac{X_{Mn}^2 X_{SiO_2}}{X_{Si} kX_{Mn-2}}} \tag{2.114}$$

where the dimensionless reaction equilibrium constant for the reaction kX_{Mn-2} is defined as (Logar, 2012, eqn 15)[1]:

$$kX_{Mn-2} = 10^{2.8\frac{X_{CaO}X_{MgO}}{X_{SiO_2}} - 1.16} \frac{M_{MnO}^2 M_{Si} M_{Fe}}{M_{Mn}^2 M_{SiO_2} M_{ISI}} \tag{2.115}$$

2.7.6.6 Equilibrium Mole Fraction of Mn in Reaction with Fe (Mn)

The equilibrium mole fraction of Mn can be determined from the following equation (Logar, 2012, eqn 17)[1]:

$$X_{Mn}^{eq} = \frac{X_{MnO}}{X_{FeO} kX_{Mn}} \tag{2.116}$$

The dimensionless reaction equilibrium constant for the reaction kX_{Mn} is determined by (Logar, 2011, eqn 18)[1] where the value of $k_{Mn\%}$ is taken as 1.8 (Turkdogan, 1996)[22]:

$$kX_{Mn} = k_{Mn\%}\frac{M_{FeO} M_{Mn} 100}{M_{MnO} M_{Fe}} \tag{2.117}$$

2.7.6.7 Equilibrium Mole Fraction of Cr in Oxidation (Cr)

The equilibrium mole fraction of Cr can be determined from the following equation (Logar, 2012, eqn 20)[1]:

$$X_{Cr}^{eq} = \frac{X_{Cr_2O_3}}{X_{FeO} kX_{Cr}} \tag{2.118}$$

The dimensionless reaction equilibrium constant for the reaction kX_{Cr} is determined by (Logar, 2012, eqn 21)[1] where the value of $k_{Cr\%}$ is taken as 0.3 (Turkdogan, 1996)[22]:

$$kX_{Cr} = k_{Cr\%}\frac{M_{FeO} M_{Cr} 100}{M_{Cr_2O_3} M_{Fe}} \tag{2.119}$$

2.7.6.8 Equilibrium Mole Fraction of P in Reaction with FeO (P)

In order to determine the equilibrium fraction of phosphorus in detail, the partition ratio of phosphorus in liquid metal and phosphorus in liquid slag as P_2O_5 was calculated by (Basu, 2007)[26]:

$$\log\frac{(\%P)}{[\%P]} = 1.97X_{CaO} + 2.0X_{FeO} - 2.04X_{SiO_2} + \frac{6713}{T_{ISI}} - 1.84 \tag{2.120}$$

2.7.7   TOPSIS Result of Optimisation of Reactor Operation

Table 2.7.20: Values of KPIs for each operation mode considered

	Outlet C %	Outlet Mn%	CapEx	OpEx	Temp	Selectivity	Emissions	Ratio
Option 1	0.335	0.721	156.558	2516.100	310.740	2914.567	6.272	10.159
Option 2	0.907	0.733	156.558	1928.600	115.771	4346.618	4.589	10.801
Option 3	0.874	0.748	183.713	1928.600	38.910	4395.910	4.594	10.720
Option 4	0.918	0.729	146.648	1928.600	139.947	4331.372	4.587	10.827

Table 2.7.21: Weights of KPIs used for Analysis

	Outlet C %	Outlet Mn%	CapEx	OpEx	Temp	Selectivity	Emissions	Ratio
Weights	0.05	0.05	0.2	0.2	0.05	0.2	0.2	0.05

Table 2.7.22: Weighted and Normalised Values of KPIs

	Outlet C %	Outlet Mn%	CapEx	OpEx	Temp	Selectivity	Emissions	Ratio
Option 1	0.0105	0.0246	0.0970	0.1203	0.0429	0.0720	0.1239	0.0239
Option 2	0.0284	0.0250	0.0970	0.0922	0.0160	0.1074	0.0906	0.0254
Option 3	0.0274	0.0255	0.1138	0.0922	0.0054	0.1087	0.0907	0.0252
Option 4	0.0288	0.0249	0.0908	0.0922	0.0193	0.1071	0.0906	0.0255

Table 2.7.23: Euclidean Distance to Best and Worst Values

	dj+	dj-
Option 1	0.0709	0.0168
Option 2	0.0335	0.1030
Option 3	0.0230	0.1096
Option 4	0.0141	0.1018

Table 2.7.24: Scores of the Options and their Ranks

	Score	Rank
Option 1	0.1918	4
Option 2	0.7548	3
Option 3	0.8265	2
Option 4	0.8787	1

2.7.8   Design of Non-detailed Reactors

For the oxidiser, air reactor and reducers 1, 2 and 3, these were modelled as two-phase, counter-current, isothermal, plug-flow reactors with kinetics given in table 2.7.25. For the hydrogen burner, this was modelled as a standard isothermal plug-flow reactor. Reactor volumes and operating conditions are given in table 2.7.26.

Table 2.7.25: Reactions, rate laws and relevant parameters for the reducers, oxidiser and air reactor.

Reaction	Rate Law	E_a (kJ mol^{-1})	k_0 (mol^{-n}m^{3n}s^{-1})
	Reducer-1 and Reducer-3		
$Fe_2O_3 + CH_4 \rightarrow 2FeO + CO + 2H_2$	$kC_{CH_4}^{0.6}(1-X_{hem.})^{2/3}$	251	1.15×10^9
$Fe_2O_3 + H_2 \rightarrow FeO + H_2O$	$kC_{H_2}^{1.16}(1-X_{hem.})^{2/3}$	59	2.24
$Fe_2O_3 + CO \rightarrow FeO + CO_2$	$kC_{CO}(1-X_{hem.})^{2/3}$	37	0.24
$FeO + CH_4 \rightarrow Fe + CO + 2H_2$	$kC_{CH_4}^{0.91}$	230	6.56×10^7
$FeO + H_2 \rightarrow Fe + H_2O$	$kC_{H_2}^{1.16}(1-X_{wus.})^{2/3}$	59	2.24
$FeO + CO \rightarrow Fe + CO_2$	$kC_{CO}(1-X_{wus.})^{2/3}$	37	0.24
$CH_4 \rightarrow C + 2H_2$	kC_{CH_4}	193	5.4×10^3
	Reducer-2		
$3Fe_2O_3 + CO \rightarrow 2Fe_3O_4 + CO_2$	$kC_{CO}(1-X_{hem.})^{2/3}$	122	847.22
$3Fe_2O_3 + H_2 \rightarrow 2Fe_3O_4 + H_2O$	$kC_{H_2}(1-X_{hem.})^{2/3}$	28	0.78
$Fe_3O_4 + CO \rightarrow 3FeO + CO_2$	$kC_{CO}(1-X_{mag.})^{2/3}$	122	847.22
$Fe_3O_4 + H_2 \rightarrow 3FeO + H_2O$	$kC_{H_2}(1-X_{mag.})^{2/3}$	28	0.78
	Oxidiser		
$Fe + H_2O \rightarrow FeO + H_2$	$kC_{H_2O}^{0.75}(1-X_{iron})^{2/3}$	27	0.122
$3FeO + H_2O \rightarrow Fe_3O_4 + H_2$	$kC_{H_2O}^{0.75}(1-X_{wus.})^{2/3}$	27	0.122
	Air Reactor		
$3FeO + 0.5O_2 \rightarrow Fe_3O_4$	$kC_{O_2}^{0.59}(1-X_{wus.})^{2/3}$	7	0.07
$2Fe_3O_4 + 0.5O_2 \rightarrow 3Fe_2O_3$	$kC_{O_2}^{0.59}(1-X_{mag.})^{2/3}$	7	0.07

Table 2.7.26: Key Design and Operation Aspects of Non-Detailed Reactor Units

0 Code	Type	Operating Temperature (K)	Operating Pressure (bar)	Volume (m^3)
AR-1	Air Reactor Unit	1433.15	1.2	30.00
OX-1	Oxidiser Unit	933.15	1.2	130.00
R-1	Reducer Unit	1245.15	1.2	80.00
R-2	Reducer Unit	1373.15	1.2	15.00
R-3	Reducer Unit	1433.15	1.2	40.00
REAC-1	Hydrogen burner	773.15	1.2	4.45

2.7.9 Mechanical Design
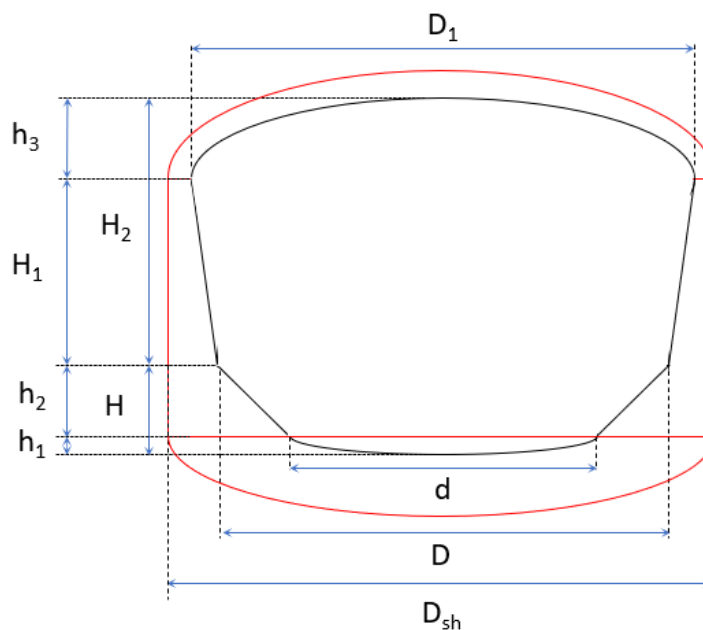
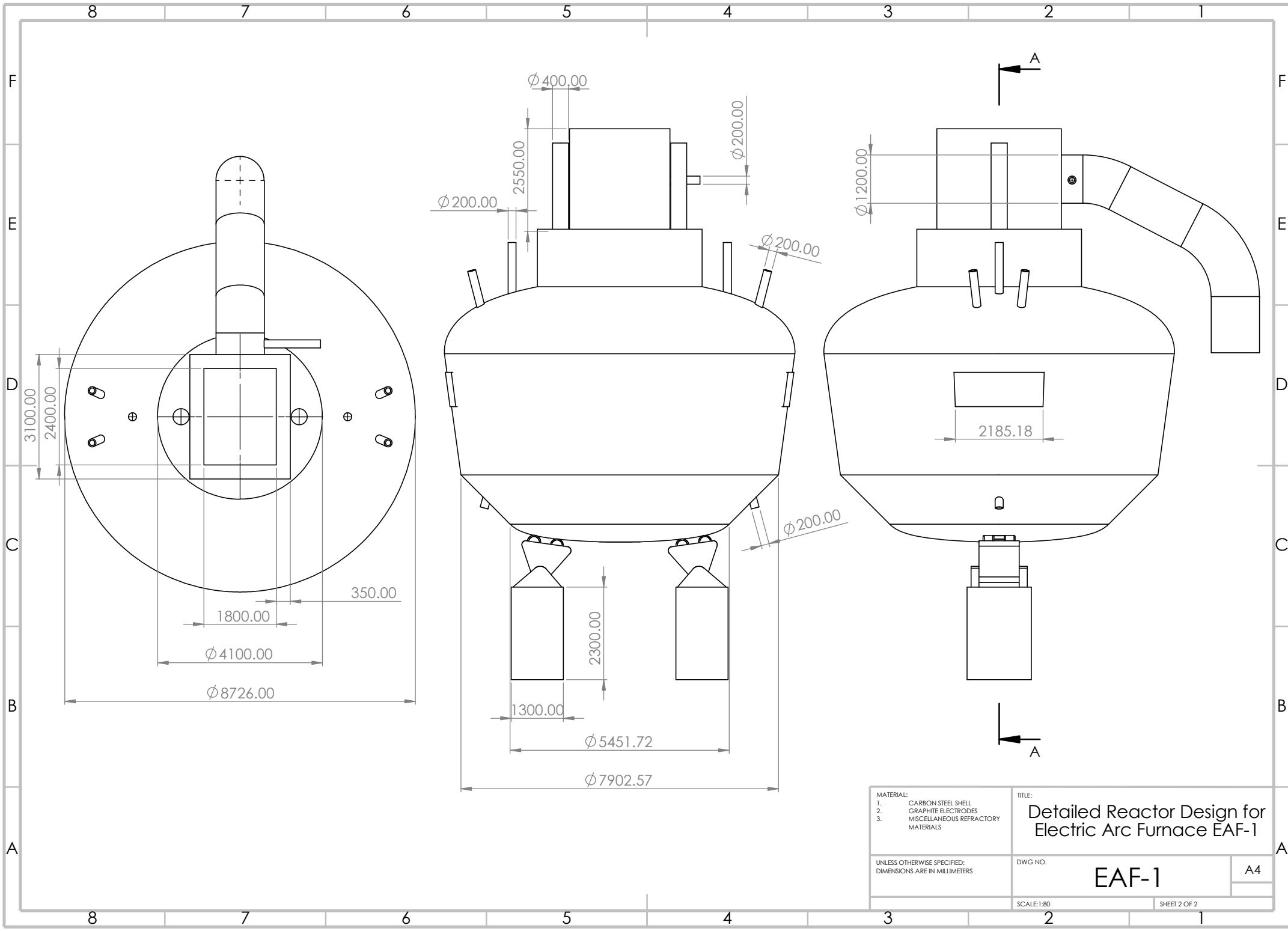**Figure 2.7.1:** Caption

Table 2.7.27: Furnace Shell Dimensions

Description	Symbol	Value	Units
Bath diameter	D	6768	mm
Total depth of bath	H	1354	mm
Height of the spherical portion	h_1	271	mm
Depth of conical portion	h_2	1083	mm
Diameter of the spherical bottom	d	4603	mm
Diameter of the reaction chamber	D_{rc}	6968	mm
Height of reaction chamber	H_1	2787	mm
Chamber of the roof	h_3	1195	mm
Total height above bath level	H_2	3983	mm
Diameter of the reaction chamber at roof skewbacks level	D_1	7526	mm
Inside diameter of the shell	D_{sh}	8168	mm

Table 2.7.28: Electrode system of EAF.

Description	Symbol	Value	Units
Electrode resistivity	δ	10	$\Omega \cdot mm^2 m^{-1}$
Coefficient	K	2.1	$A\ cm^{-2}$
Linear current	I_{total}	71,462	A
Current for each electrode	I	17,867	A
Diameter of central electrode	d	400	mm

Table 2.7.29: Transformer power and furnace productivity.

Description	Symbol	Value	Units
Transformer power	P_{ap}	80	MVA
Average power consumed during melting period	P_{av}	64	MVA
Useful power consumed during melting period	P_u	48960	kW
Upper voltage taps of secondary voltage	V_{upper}	646	V
Lower voltage taps of secondary voltage	V_{lower}	163	V

Ø400.00

Ø200.00

2550.00

Ø200.00

Ø200.00

Ø200.00

Ø1200.00

A

A

3100.00

2400.00

350.00

1800.00

Ø4100.00

Ø8726.00

2300.00

1300.00

Ø5451.72

Ø7902.57

2185.18